

INFORMATION TO USERS

This manuscript has been reproduced from the microfilm master. UMI films the text directly from the original or copy submitted. Thus, some thesis and dissertation copies are in typewriter face, while others may be from any type of computer printer.

The quality of this reproduction is dependent upon the quality of the copy submitted. Broken or indistinct print, colored or poor quality illustrations and photographs, print bleedthrough, substandard margins, and improper alignment can adversely affect reproduction.

In the unlikely event that the author did not send UMI a complete manuscript and there are missing pages, these will be noted. Also, if unauthorized copyright material had to be removed, a note will indicate the deletion.

Oversize materials (e.g., maps, drawings, charts) are reproduced by sectioning the original, beginning at the upper left-hand corner and continuing from left to right in equal sections with small overlaps. Each original is also photographed in one exposure and is included in reduced form at the back of the book.

Photographs included in the original manuscript have been reproduced xerographically in this copy. Higher quality 6" x 9" black and white photographic prints are available for any photographs or illustrations appearing in this copy for an additional charge. Contact UMI directly to order.

UMI

A Bell & Howell Information Company
300 North Zeeb Road, Ann Arbor MI 48106-1346 USA
313/761-4700 800/521-0600

The Projector Basis Method for Electronic Bandstructure
Calculations

A Dissertation

Presented to The Faculty of the Department of Physics

The College of William and Mary

In Partial Fulfillment

Of the Requirements for the Degree of

Doctor of Philosophy

By

Christopher Haas

August 1996

UMI Number: 9720974

**Copyright 1997 by
Haas, Christopher**

All rights reserved.

**UMI Microform 9720974
Copyright 1997, by UMI Company. All rights reserved.**

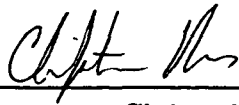
**This microform edition is protected against unauthorized
copying under Title 17, United States Code.**

UMI
300 North Zeeb Road
Ann Arbor, MI 48103

APPROVAL SHEET

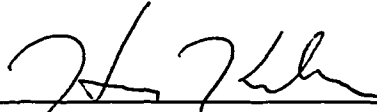
This dissertation is submitted in partial fulfillment
of the requirements for the degree of

Doctor of Philosophy.



Christopher Haas

Approved, August 1996



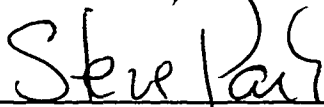
Henry Krakauer



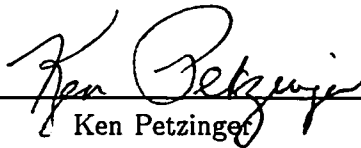
Jack Kossler



Dennis Manos



Steve Park



Ken Petzinger

To Ellen

Contents

Acknowledgments	vi
List of Tables	vii
List of Figures	viii
Abstract	ix
Chapter 1 Introduction and Background Theory	2
1.1 Objective	2
1.2 Standard Methods of Calculation	4
1.3 Pseudopotentials	7
Chapter 2 The Projector Basis Method	11
2.1 Development of the Hamiltonian	12
2.2 The Projector Basis Method	15
2.3 Implementing the Projector Basis Method	20
Chapter 3 Test Calculations	24
3.1 GaAs	25
3.2 Carbon	32
3.3 Copper	35
3.4 $\text{Bi}_2\text{Sr}_2\text{Ca}_1\text{Cu}_2\text{O}_8$	40
Chapter 4 Electrides	45
4.1 Introduction	45
4.2 $\text{Cs}^+(15\text{-crown-5})_2\cdot\text{e}^-$	48
4.3 $\text{Li}^{-1}(\text{crypt-2.1.1})\cdot\text{e}^-$	56
Chapter 5 Conclusion	80

Bibliography

82

Vita

88

Acknowledgments

I would like to thank Henry Krakauer for the guidance and support needed to make this project possible. Thanks also to all of my friends at William and Mary who made my stay there an enjoyable and growing experience. A special thanks goes to Ellen Haas, for encouraging me to finish the project in a timely manner.

List of Tables

3.1	Properties of the pseudopotentials used in the GaAs calculations	26
3.2	Theoretical and experimental results for GaAs	27
3.3	Details of the local basis used in the GaAs comparison runs	29
3.4	Comparison of the GaAs results for different local bases	30
3.5	Comparison of various eigenvalue spectrums for diamond	33
3.6	Comparison of various theoretical eigenvalue spectrums for fcc copper . . .	36
3.7	Details of the local basis used in the BSCCO calculation	42
4.1	Details of the local basis used for the crown ether electrider	50
4.2	Dispersion of the states near E_F for the crown ether electrider	50
4.3	Details of the local basis used in the Li cryptand calculation	58
4.4	Brillouin zone k -dispersions for the Li cryptand	61

List of Figures

1.1	Copper pseudo-wave functions for the configuration $3d^{10}4s^84p^2$	9
3.1	Comparison of various GaAs charge densities in the $[1\bar{1}0]$ plane	31
3.2	Comparison of the diamond DOS from the LAPW and mixed basis codes	34
3.3	Energy bands for fcc copper along selected high-symmetry directions	39
3.4	Unit cell of the bismuth superconductor	41
3.5	Fermi surface of BSCCO	44
4.1	Structure of a molecule of the cesium crown ether electride	49
4.2	Schematic representation of the electronic energy bands for an electride	51
4.3	Sequence of charge isosurfaces for the cesium crown ether	53
4.4	Cesium crown ether potential shown as both a perspective surface and contour plot	54
4.5	Structure of a molecules of the K-2.2.2 cryptand	57
4.6	Cryptand charge density at Γ , with a density of 1.5×10^{-4} e/a.u. ³	62
4.7	Cryptand charge density at Γ , with a density of 2.0×10^{-4} e/a.u. ³	63
4.8	Cryptand charge density at Γ , with a density of 2.5×10^{-4} e/a.u. ³	64
4.9	Cryptand charge density at Γ , with a density of 3.0×10^{-4} e/a.u. ³	65
4.10	Combined cryptand electride bands at Γ , at a density of 2.0×10^{-4} e/a.u. ³	67
4.11	Combined cryptand electride bands at Γ , at a density of 3.0×10^{-4} e/a.u. ³	68
4.12	Comparison of the electride band charge densities of the first two bands at Γ and L , at a density of 3.0×10^{-4} e/a.u. ³	69
4.13	Comparison of the electride band charge densities of the first two bands at Γ and L , at a density of 4.5×10^{-4} e/a.u. ³	70
4.14	Cryptand charge density at Γ , at a density of 1.5×10^{-4} e/a.u. ³	72
4.15	Cryptand charge density at Γ , at a density of 3.5×10^{-4} e/a.u. ³	73
4.16	Cryptand charge density at Γ , at a density of 4.5×10^{-4} e/a.u. ³	74
4.17	A sequence of isosurface contours of the potential in the lithium cryptand	75

4.18 Comparison of a potential isosurface with the charge density at Γ (3.0×10^{-4} e/a.u. ³)	76
4.19 Comparison of a potential isosurface with the charge density at Γ (3.0×10^{-4} e/a.u. ³)	77
4.20 Comparison of a potential isosurface with the charge density at Γ (4.5×10^{-4} e/a.u. ³)	78

Abstract

Over the last several decades, two methods have emerged as the standard tools for the calculation of electronic band structures. These methods, the Car-Parinello plane wave method and the linear augmented plane wave method (LAPW), each have strengths and weaknesses in different regimes of physical problems. The Car-Parinello algorithm is ideal for calculations with soft pseudopotentials and large numbers of atoms. The LAPW method, on the other hand, easily handles all-electron and hard-core pseudopotential calculations with a small number of atoms. The projector basis method, presented here, is a hybrid mixed basis method which allows the calculation of moderately large (~ 200) numbers of atoms represented by hard pseudopotentials. This method will then be used to calculate two members of a relatively new class of materials, called electriles, in which the anion has been replaced with a localized electron.

The Projector Basis Method for Electronic Bandstructure
Calculations

Chapter 1

Introduction and Background

Theory

1.1 Objective

First principles electronic structure calculations are a very important tool in the understanding of condensed matter systems. These calculations are capable of computing a variety of ground state and equilibrium properties, such as lattice constants, bulk moduli, and phonon frequencies, without approximations to the shape of the potential or the geometry of the crystalline system.

Accurate calculations of the electronic structure yield information about the spatial and energetic distribution of charge, which includes information such as where bonding occurs and what type of atomic character it has. In the case of the high temperature superconductors, this information can yield clues as to what structural features differentiate their normal state properties from those of other materials. In the case of materials like the electrides, unusual electronic structures can be described. Hence these calculations

give a better understanding of both the theoretical problems and the experimental puzzles surrounding a wide variety of materials.

The Car-Parinello (CP) style plane wave method [1, 2] and the linear augmented plane wave (LAPW) method [3] epitomize the current state of the art in electronic structure calculations. Plane wave methods, with standard pseudopotentials, are capable of performing calculations on systems with as many as a few hundred atoms, but have difficulty with systems containing transition metals or first row elements. A new type of pseudopotential, the ultrasoft pseudopotential, may alleviate the situation somewhat, but at the cost of additional complications. Plane wave codes are currently used to perform *ab initio* molecular dynamics studies of crystalline and non-crystalline materials and to study surface properties.

The LAPW method, on the other hand, is capable of highly accurate calculations on systems containing almost any element, but at the expense of computer storage and CPU time: the LAPW method is generally restricted to about thirty atoms. It has successfully performed calculations on ferroelectrics, and it correctly models the surface and bulk properties of many different systems. The strength of the LAPW method lies in its ability to perform calculations on systems containing transition metal and first row elements.

The objective of this thesis is to implement the *projector basis technique*, a method that incorporates the strengths of the LAPW and the Car-Parinello methods into a single method. This method is designed to increase the efficiency of LAPW style methods so that larger systems can be studied. Currently, calculations for systems with up to 200 atoms have been performed.

1.2 Standard Methods of Calculation

In the projector basis technique, as with other methods for calculating electronic structure, certain approximations must be made to simplify the problem. The first simplification, the density functional theory (DFT) of Hohenberg and Kohn [4, 5], is used to reduce the many-body Hamiltonian to a single particle Hamiltonian by approximating the many-body exchange-correlation potential with a single particle potential. This reduction is carried out using as input only the types of atoms in the system and their positions; hence, these methods are called *ab initio* methods. Hohenberg and Kohn [4] showed that the Hamiltonian is a functional of the charge density n , and that the total energy is minimized when n is the true charge density. Kohn and Sham [5] then introduced the local density approximation (LDA) to convert the DFT Hamiltonian to a single particle Schrödinger equation. The LDA introduces the exchange-correlation potential V_{xc} , which incorporates the many-body effects, and, unlike Hartree-Fock theory [6], is a local, single particle potential. The main drawback to density functional theory is that the form of V_{xc} is not known. The approximation that is used is that V_{xc} for a small region of space is assumed to be constant, and its value is taken from the homogeneous electron gas at the same charge density. The LDA is exact for systems in which the charge density is slowly varying. For a wide variety of other systems, the LDA generally gives remarkably good results for the band structure, total energy, and charge density. However, in semiconductors it is known to underestimate band gaps by ten to thirty percent and lattice parameters by one to two percent. The LDA is also known to fail in highly correlated Mott-Hubbard insulators such as La_2CuO_4 . DFT will be discussed in greater detail in the next chapter.

There are many different techniques for solving the Kohn-Sham equations. The standard technique is to use a variational basis to solve the equations self-consistently, which allows the solution to be refined iteratively. In general, the major difference between

the methods is the representation of the wave function.

A first choice for a representation, or basis, of the wave functions is one which is complete, e.g., plane waves. However, a plane wave basis has difficulties with localized electronic core states, which require large numbers of plane waves to represent. So, the strong atomic potentials are usually replaced with much weaker pseudopotentials, creating pseudo-atoms. While the chemical properties of the pseudo-atom are identical to those of the original atom, the corresponding pseudo-wave functions are much more conducive for calculations using plane waves, due to their smoothness. Even with pseudopotentials, however, plane waves are not efficient when there is a great deal of empty space in the unit cell, or when localized valence orbitals are present, e.g., first row atoms and transition metals. Transition metals, for example, have narrow *d*-like valence states, and the resulting pseudopotentials and pseudo-wave functions are strong and rapidly varying, which are difficult to represent by plane waves. Even with this drawback, the pseudopotential plane wave method is one of the more popular calculational methods. Pseudopotentials will be discussed more fully below.

A method for fully exploiting the properties of a plane wave basis was developed by Car and Parinello [1]. In conventional electronic structure methods, a matrix is diagonalized to give the coefficients of the basis functions that solve the problem. In the Car-Parinello method, the basis functions (and possibly the atomic coordinates) are considered to be fictitious classical particles. By setting up a Lagrangian, the equations of motion can be solved by standard methods (see, for example, [2]), such as simulated annealing or the conjugate gradient method, *without* diagonalizing a matrix. This allows both charge relaxation and geometrical relaxation to occur simultaneously. With the exception of the orthogonalization step which is an $O(N_A^3)$ process (N_A is the number of atoms), this method is $O(N_A^2 \log(N_A))$ (due to FFTs), which scales much better than other methods. Since the

basis is a simple one, computing quantities such as kinetic energy and forces is much simpler than in other methods.

When the Car-Parinello method is implemented with the use of pseudopotentials, a very powerful method results. This type of method is capable of calculating systems with hundreds of atoms, though calculating systems with first row or transition metal atoms is still difficult. Work is being done, though, on modifying the pseudopotentials so that these other systems can be treated [7-9].

Another set of methods results from augmenting the plane waves with functions designed to represent the atomic states. Consider dividing space by non-overlapping spheres, called muffin tin (MT) spheres, which are centered on the atoms. Inside the MT spheres, the wave function is represented by atomic-like orbitals, and outside by plane waves. One such method is the augmented plane wave method (APW) [10, 11]. One variation on the APW method which is in wide use is the linear augmented plane wave method (LAPW) [12-14]. The key difference between the APW and LAPW methods is the matching of the different basis representations at the MT boundary. In the APW method, the wave function has discontinuous derivatives, while in the LAPW method, the first derivatives are continuous. The APW-style methods tend to be more accurate than the other methods. The addition of atomic-like orbitals allows the wave function to accurately represent the core levels, while the plane waves provide an efficient basis to represent the wave function in the interstitial region between the MT spheres. However, the APW-style codes, which scale as $O(N_A^3)$, are much more complicated to implement than plane wave codes.

The time-limiting step in all of these methods is applying the Hamiltonian operator to the wave function [15]. In plane wave methods, the potential operates on the wave function in real space while the kinetic energy operates in reciprocal space, and the timing for each of these operations scales linearly. Performing the FFT to take the wave function from

reciprocal space to real space takes $O(N_{PW} \log N_{PW})$ operations. Since these operations must be done for each electronic energy band, and the number of bands scales linearly with the number of atoms, plane wave methods scale as $O(N_A^2 \log N_A)$. In the APW-style methods, the application of the Hamiltonian to the wave function scales as $O(N_A^2)$ per band, which makes them $O(N_A^3)$ methods. All of these methods also require that the eigenvectors be orthogonal. This step additional takes $O(N_A^3)$ time, but is not a limiting step until the number of atoms becomes large.

The projector basis method is an example of a mixed basis method. In these type of methods, the wave function is represented by two or more different types of basis functions in the same region of space. The projector basis method utilizes both plane waves and localized, non-overlapping atomic-like orbitals. The plane waves are treated the same as in a CP method and the local functions are handled quickly by a special technique, so that the $O(N_A^2 \log N_A)$ scaling is preserved. With the addition of the atomic-like orbitals, this method has accuracy comparable to that of the LAPW method for first row and transition metal atoms.

1.3 Pseudopotentials

In the 1960's, it was found that the full Hamiltonian for a system could be replaced with an effective Hamiltonian whose spectrum contained only the valence electron states [16, 17]. This was done by replacing the potential with a "pseudopotential" which projects the core electron states out of the spectrum. The main properties of these potentials are that the eigenvalues for a given electronic configuration are reproduced, i.e. the scattering properties for electromagnetic waves for particles like e^- are reproduced, and that the real and pseudo-wave functions are equal outside a cutoff radius r_c .

Developments in the late 1970's by Hamann, Schlüter and Chiang [18] (HSC), and

also by Kerker [19], introduced first-principles pseudopotentials. Hamann *et al* found two requirements on existing pseudopotentials that allowed them to be more transferable from isolated atomic situations to crystalline environments, and also made them softer (i.e., representable by smaller numbers of plane waves). The first is norm conservation: the integrated charge for $r > r_c$ should agree for the real and pseudo-charge. This guarantees that the electrostatic potential is the same for each atom outside r_c . The second is that for $r > r_c$ the logarithmic derivatives and the first energy derivatives of the real and pseudo-wave functions should be equal. This helps to insure that the pseudo-atom's core, the region inside r_c , reproduces the scattering properties of the atomic core with minimum error.

HSC pseudopotentials are produced by replacing the (possibly relativistic) atomic potential with an intermediate potential using a parameterized cutoff function f . Using this potential, this intermediate pseudo wave function is calculated and modified with a second cutoff function g to produce the final, nodeless wave function with the properties stated above. Using this pseudo wave function, the Schrödinger equation is inverted—the pseudo-wave function is nodeless—to give the final pseudopotential.

Kerker pseudopotentials also begin with the (possibly relativistic) wave functions and potentials from an atomic calculation. Kerker's method matches the exact wave function with a parameterized analytic form for $r \leq r_c$. Matching the derivatives of the wave functions to second order, the resulting Schrödinger equation is inverted, as in the HSC method. The pseudopotentials created by this method are of the same quality as the HSC potentials, but are simpler to create.

Pseudo-wave functions for the $3d$, $4s$ and a partially occupied $4p$ levels of a copper atom from a Kerker-style calculation are shown in Fig. 1.1, along with the corresponding all-electron orbitals. Like the HSC pseudopotentials, these are non-local, being l -dependent for $r \leq r_c$. For $r > r_c$, Kerker potentials are strictly local. Another point that can be seen

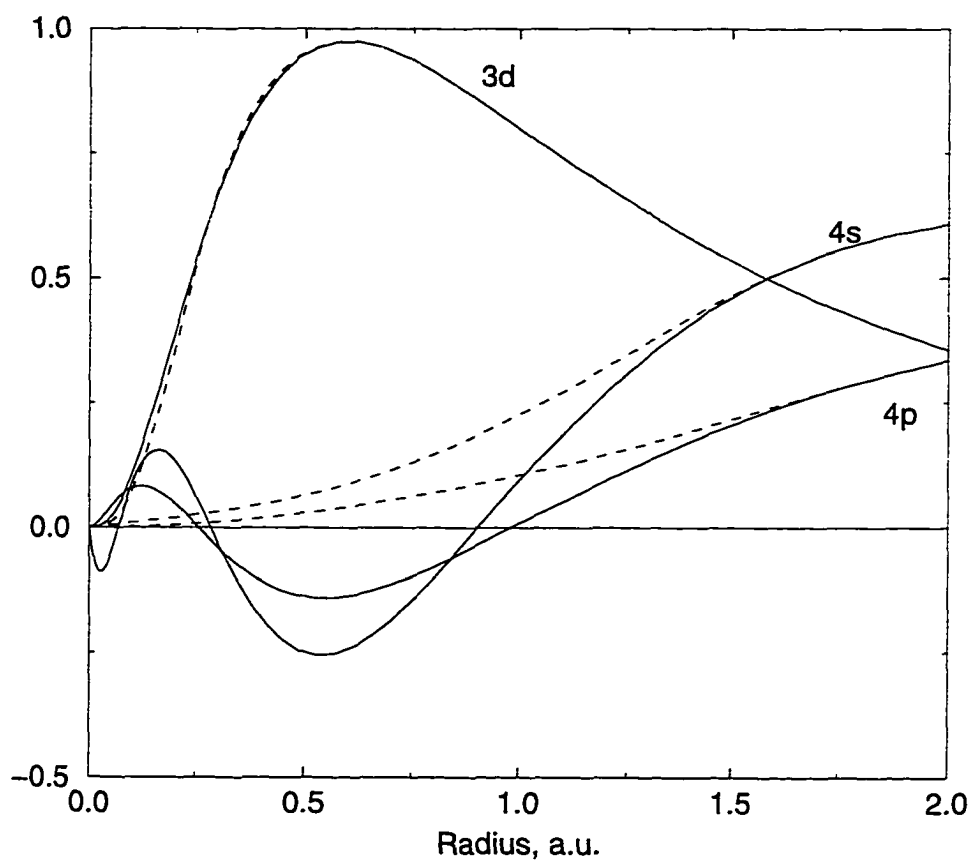


Figure 1.1: Copper pseudo-wave functions for the configuration $3d^{10}4s^{0.8}4p^{0.2}$. The solid line represents the all-electron wave function and the dashed line represents the pseudo-wave function. r_c is 1.49 for the s and p wave functions and 0.25 for the d wave function. The d function is said to be hard, while the s and p functions are soft.

from the d function in Fig 1.1 is that the smaller the value for r_c , the harder (i.e. more rapidly varying) the pseudo-wave function, and hence the pseudopotential, is. The s and p functions are said to be soft, which implies that they are easier to represent with a plane wave basis.

The choice of r_c can be very important to a band structure calculation. Plane wave methods require exceptional computational effort for hard potentials, so the size of r_c is maximized for these methods. For the LAPW and projector basis methods, however, hard pseudopotentials represent no added difficulty, so r_c can be chosen to maximize the quality and transferability of the pseudopotential. In these methods, the pseudopotential simply represents a computational simplification of the original problem, since the core electrons do not need to be calculated.

The remainder of the dissertation is organized as follows. Chapter 2 introduces the theory behind the projector basis method, and the Chapter 3 gives the results of several simple calculations to validate the method, as well as a calculation on the high- T_c cuprate $\text{Bi}_2\text{Sr}_2\text{Ca}_1\text{Cu}_2\text{O}_8$ to show how the code scales for large systems. The fourth chapter details two large scale calculations on the electrides $\text{Cs-(15C6)}e^-$ and $\text{Li-(crypt-2.1.1)}e^-$. The final chapter contains the summary and concluding remarks.

Chapter 2

The Projector Basis Method

All of the band structure methods presented so far have one major feature in common, that in a given region of space, there is only one representation for the wave function. In the LAPW method, for example, the wave function in the interstitial region (outside the muffin tin spheres) is expanded only in plane waves, while within the muffin tin spheres it is expanded in atomic-like orbitals. By contrast, in a mixed basis method, a given region of space can have more than one set of basis functions. The advantage of a mixed basis method is that the different sets of functions can be tuned to different aspects of the system being calculated. Plane waves are very good at representing the slowly changing behavior of the charge and potential both in the interstitial region and inside the muffin tin. Atomic-like orbitals can then be added in the muffin tin spheres to better represent tightly bound states.

The reason mixed basis methods have not been popular is the complexity of the equations used to perform the calculation. Normal basis sets for these calculations consist of a large number of plane waves and a small number of atomic-like orbitals. In order to compute the matrix elements between the two representations, integrals between each

atomic orbital and each plane wave must be computed of all space for each band and k point. As the system size increases, this quickly makes the calculations unmanageable, as will be shown below.

The projector basis method [15] provides a means of doing these integrals efficiently. The remainder of this chapter describes the theory and implementation of the projector basis method. The first section outlines the reduction of the many-body Hamiltonian to a single-particle Schrödinger equation, and the second section describes projector basis method. The final section describes the details of the basis functions and the eigenvalue solver.

2.1 Development of the Hamiltonian

The full Hamiltonian for a crystalline system is

$$H = - \sum_i \frac{\hbar^2}{2m} \nabla_i^2 + \frac{1}{2} \sum_{i \neq j} \frac{e^2}{|r_i - r_j|} - \sum_{i, \alpha} \frac{Z_\alpha e^2}{|r_i - R_\alpha|} - \sum_\alpha \frac{\hbar^2}{2m_\alpha} \nabla_\alpha^2 + \frac{1}{2} \sum_{\alpha \neq \beta} \frac{Z_\alpha Z_\beta e^2}{|R_\alpha - R_\beta|}, \quad (2.1)$$

where i and j label electrons and α and β label nuclei. The first three terms are those due to the electrons and their interaction with the nuclei: the kinetic energy, the electron-electron interaction, and the electron-nuclei interaction. The last two terms deal with the nuclei alone: the kinetic energy of the nucleus and the nuclear-nuclear interaction. In the Born-Oppenheimer approximation, the atomic positions are fixed, implying that the nuclear kinetic energy and potential energy are constant, which removes these terms from the Hamiltonian. This also allows the Coulomb potential due to the nuclei to be considered an external potential. The electronic Hamiltonian can then be rewritten as

$$H = - \sum_i \nabla_i^2 + \frac{1}{2} \sum_{i \neq j} \frac{1}{|r_i - r_j|} + V_{ext}, \quad (2.2)$$

using Rydberg atomic units of $\hbar = 1$, $e = 1$ and $m = 1/2$.

The density functional theory of Hohenberg and Kohn [4] is used to obtain the ground state charge density and energy of Eq. (2.2). They proved two theorems which form the basis of density functional theory (DFT). The first theorem is that the ground state total energy is a unique functional of the ground state charge density,

$$E_v[n] = \int v_{ext}(\vec{r})n(\vec{r})d\vec{r} + \frac{1}{2} \int \frac{n(\vec{r})n(\vec{r}')}{|\vec{r}-\vec{r}'|}d\vec{r}d\vec{r}' + T_s[n] + E_{xc}[n]. \quad (2.3)$$

Here, $n(\vec{r})$ is the charge density,

$$n(\vec{r}) = \sum_{i=1}^N |\Psi_i(\vec{r})|^2 \quad (2.4)$$

$v_{ext}(\vec{r})$ is the external potential, E_{xc} is the exchange-correlation potential. $T_s[n]$ is the kinetic energy functional for a fictitious noninteracting electron gas, with the charge density of the real system,

$$T_s[n] = \int (\nabla\Psi^*) \cdot (\nabla\Psi)d^3r. \quad (2.5)$$

Note that $T_s[n]$ is short hand for $T_s[n(\vec{r})]$. The second theorem is that there exists a unique value for $n(\vec{r})$ such that the total energy is minimized.

Kohn and Sham [5] showed that the solution to Eq. 2.3 could be obtained by variation of the total energy with respect to the single particle wave functions that describe the fictitious noninteracting system. The approximation used, the local density approximation (LDA), was to write the exchange correlation energy in the form of that of a non-interacting electron gas,

$$E_{xc}[n] = \int n(\vec{r})\varepsilon_{xc}(n(\vec{r}))d\vec{r}. \quad (2.6)$$

Since $\varepsilon_{xc}(n(\vec{r}))$ is not known, it is replaced with the exchange-correlation potential of the uniform interacting electron gas, while $n(\vec{r})$ is the charge density for the inhomogeneous problem at hand. The corresponding exchange correlation potential is

$$V_{xc}(n) = \frac{d(n\varepsilon_{xc}(n))}{dn}. \quad (2.7)$$

As stated earlier, the LDA does a remarkably good job for a large class of materials. Still, there is a continuing effort to improve upon the LDA results (see, for example, [7, 20, 21]). The form of the exchange correlation potential used here is due to Hedin and Lundqvist [22].

The resulting Euler-Lagrange equations must then be solved self-consistently:

$$[-\nabla^2 + V_{ext} + V_H(\vec{r}) + V_{xc}] \Psi_i(\vec{r}) = \varepsilon_i \Psi_i(\vec{r}) \quad (2.8)$$

where the Hartree potential,

$$V_H(\vec{r}) = \int \frac{n(\vec{r}')}{|\vec{r} - \vec{r}'|} d\vec{r}' \quad (2.9)$$

and the exchange correlation potential,

$$V_{xc}(n) = \frac{d(n\varepsilon_{xc}(n))}{dn}, \quad (2.10)$$

are both functionals of the charge density. Equation (2.8) is the single particle Schrödinger equation for the fictitious system with an effective potential. All of the many-body electron interactions have been incorporated into the exchange correlation potential.

The problem of calculating the band structure of a given crystalline system is reduced to solving the two equations, Eq. (2.8) and Eq. (2.4), self-consistently. The solution proceeds as follows. First, guess a form for the charge density, n . From this n , obtain V_H and V_{xc} and solve Eq. (2.8). This is usually done using a variational basis to represent the single particle wavefunctions, leading to a matrix eigenvalue equation. Diagonalizing this matrix Hamiltonian yields a new set of eigenvalues and eigenvectors, which are then used to calculate a new charge density. This procedure is iterated until the change of the charge density from one iteration to the next is below a given tolerance.

2.2 The Projector Basis Method

The technique for computing the matrix elements between the local representation and the plane wave representation is usually the bottleneck in a mixed basis method. The projector basis method concentrates on removing this problem and at the same time achieving an all around scaling similar to a Car-Parinello method.

The basis in this method is given by

$$\Psi = \sum a_i e^{i(\vec{k} + \vec{G}) \cdot \vec{r}} + \sum b_i u_i(\vec{r}) = \Psi_{pw} + \Psi_{MT}, \quad (2.11)$$

where the \vec{G} are reciprocal lattice vectors and the u_i are local non-overlapping basis functions centered on the nuclei. In a more convenient notation, Eq. (2.11) can also be written

$$\Psi = \sum c_i \phi_i. \quad (2.12)$$

The plane waves extend over the entire unit cell, and are limited in number by a kinetic energy cut-off. The local basis functions are defined as radial functions times spherical harmonics. The properties of the local basis functions will be described more fully in the next section, but the main points to keep in mind are that the local functions vanish smoothly at the surface of the MT sphere and that the number of local functions is much smaller than the number of plane waves.

Minimizing Eq. 2.3 with respect to the c_i 's of Eq. 2.12, with the condition

$$\int \Psi_{m'}^* \Psi_m = \delta_{m',m}, \quad (2.13)$$

the resulting Euler-Lagrange equations take the form of the generalized matrix eigenvalue equations

$$[H_{i,j} - \varepsilon_m O_{i,j}] c_j^m = 0 \quad (2.14)$$

where the subscript m is the band label, and the Hamiltonian and overlap matrices are defined by

$$H_{i,j} = \langle \phi_i | H | \phi_j \rangle \quad (2.15)$$

and

$$O_{i,j} = \langle \phi_i | \phi_j \rangle. \quad (2.16)$$

Consider one of the Hamiltonian matrix elements from Eq. 2.15. If X is a generic operator in the Hamiltonian, then the matrix element between a plane wave and a local function would look like

$$\langle \Psi_{pw} | X | \Psi_{MT} \rangle = \int e^{-i(\vec{k} + \vec{G}) \cdot \vec{r}} X(\vec{r}) u_j(\vec{r}) d\vec{r}. \quad (2.17)$$

The time to calculate this integral for one iteration scales as $N_{pw} N_{loc} N_{k-points} N_{bands} N_{atoms}$. This is why mixed basis methods are not normally employed for solving band structure problems.

In plane wave methods, this problem is solved by never explicitly forming $H_{i,j}$. Plane wave methods solve $H_{i,j} - \epsilon O_{i,j}$ by iteratively minimizing

$$[H - \epsilon] \Psi_{PW}^{trial} = \delta R \quad (2.18)$$

for each band. Each subsequent Ψ is obtained by integrating the constrained equations of motion, rather than by directly minimizing $H_{i,j}$ (see, for example, [2]). Thus the scaling of plane wave methods is dominated by the application of the real space potentials to the wavefunction, for which FFT's must be performed. The projector basis method uses a different set of tricks to achieve a similar performance, as will be shown later.

The basis defined in Eq. (2.11) has several properties that make the integral in Eq. (2.17) tractable. Since the u_i vanish at the surface of the MT sphere, the u_i for

different spheres are non-overlapping. Thus the integral (on a real space mesh) becomes an integral over a single MT sphere. Rather than trying to decompose Ψ_{pw} inside the MT sphere, we perform an FFT to obtain Ψ_{pw} on the real space FFT mesh. However, the FFT mesh is different from the real space mesh used by the local functions. What is needed is an efficient method of integrating over the two different meshes.

These two real space meshes are not compatible meshes. The FFT mesh is a mesh of evenly spaced points through out the unit cell, while the radial mesh for the local basis functions is a logarithmic mesh centered in the muffin tin sphere (the logarithm of each of the mesh points is evenly spaced). It is possible to interpolate from the FFT mesh to the radial mesh. The essence of the projector basis method is to use a set of fitting functions to mediate operations between the two meshes.

These fitting functions, or projector functions, are a real-space representation of Ψ_{PW} obtained from the real space FFT mesh, i.e. ψ_{PW} , inside the MT sphere. They are not designed to be a complete representation of the real space FFT mesh, but a representation that is sufficiently accurate within the relevant MT sphere only. The plane waves at \vec{r}_h are expanded as

$$\psi_h^{PW} = \sum_i a_i e^{i(\vec{k} + \vec{G}) \cdot \vec{r}_h} = \sum_j d_j f_j(\vec{r}_h) \quad (2.19)$$

where the projector functions f_j are defined as

$$\begin{aligned} L &= 0, \dots, l_{max} \\ f_j(\vec{r}) &= r^p Y_{LM}(\vec{r}), \text{ where } p = L, L+2, \dots, p_{max}. \\ M &= -L, \dots, L \end{aligned} \quad (2.20)$$

Here, the subscript j simply counts the projector functions. This form was chosen because the asymptotic form for a plane wave is powers of r times the spherical harmonics Y_{LM} .

The largest possible l_{max} is determined by the number of FFT points inside the MT sphere, though it can be chosen to be smaller. p_{max} is generally chosen to be same as l_{max} , and l_{max} is typically chosen to be in the same range as in an LAPW calculation, which is in the range 8-10.

Fitting the projector functions to the plane waves can be done either by a least squares technique or by a constrained fit, but generally the least squares fit is chosen as it uses a slightly smaller number of basis functions. The fit is performed simultaneously for all the FFT points inside the MT sphere, yielding a fitting matrix $A_{j,k}$, where j labels the projector function and k labels the FFT point. Using the A matrix, the coefficients d_j in Eq. 2.19 are

$$d_j = \sum_k \psi_{PW,k}^* A_{j,k}^T. \quad (2.21)$$

Thus the fit can be done once and used many times as ψ_{PW} changes, though in practice the A matrix is recalculated on each self-consistent iteration, to avoid the cost of having to store it between iterations.

The matrix elements of Eq. 2.17 can now be rewritten using the A matrix as

$$\langle \Psi_{PW} | X | \Psi_{MT} \rangle = \sum_j \sum_k \psi_{PW,k}^* A_{j,k}^T \left[\int f_j(\vec{r}) X(\vec{r}) u_i(\vec{r}) d\vec{r} \right] b_i. \quad (2.22)$$

The integral

$$X_{j,i} = \int f_j(\vec{r}) X(\vec{r}) u_i(\vec{r}) d\vec{r} \quad (2.23)$$

may be carried out by a straight forward quadrature on the radial MT mesh and a simple angular momentum integral. The final form for Eq. 2.17 is

$$\langle \Psi_{PW} | X | \Psi_{MT} \rangle = \sum_{i,j,k} \psi_{PW,k}^* A_{j,k}^T X_{j,i} b_i = \sum_{i,k} \psi_{PW,k}^* T_{k,i} b_i. \quad (2.24)$$

All of the terms in the Hamiltonian can be added together into a single T matrix without loss of information. Though the combined T matrix could be represented on the computer

as one large square matrix of size $N_{pw} + N_{loc}$, it is convenient to represent it as three submatrices, one each of sizes N_{pw}^2 , $N_{pw} \times N_{loc}$, and N_{loc}^2 . For example,

$$\langle \Psi_{PW} | X | \Psi_{PW} \rangle = \sum_{k,k'} \psi_{PW,k'}^* T_{k,k'} \psi_{PW,k} \quad (2.25)$$

would be stored separate from the PW-MT and MT-MT pieces.

The ability of T to represent matrix elements in the MT sphere,

$$\langle \Psi_i | X | \Psi_j \rangle = \Psi_i T_{i,j} \Psi_j, \quad (2.26)$$

is dependent on the A matrix being a robust mapping from the plane waves to the projector functions. The quality of the fit provided by A can be improved most easily by increasing the number of points in the FFT mesh. For a given mesh, however, the maximum angular momentum character the projector functions can match (see Eq. 2.20) is a function of the number of FFT points in the MT sphere, and the actual l_{max} can be varied up to that maximum. The number of points on the radial MT mesh affects the quality of the T matrix: the larger the number of points, the more accurate the integrations in Eq. 2.23 are. The density of these meshes is comparable to that in LAPW calculations, and adds very little to the cost of the calculation. The T matrices are the heart of the projector basis method, since they provide an $O(N_A)$ method for minimizing $\delta R = [H - \epsilon O] \Psi_{trial}$. With the T matrix precalculated, the calculation of δR is now simply two matrix-vector multiplications. It should be noted that the matrices H and O are never explicitly calculated or stored. Using the T matrix, the most time consuming part of the eigenvalue solver is doing FFTs, which in turn means that the projector basis method scales like a Car-Parinello plane wave method.

Due to the overhead of calculating the T matrices, other methods, such as the LAPW method, are faster at calculations for systems containing less than 5 – 10 atoms. For larger systems, however, the projector basis method is significantly faster. For example,

the calculation of a single iteration on the tetragonal unit cell of $\text{Bi}_2\text{Sr}_2\text{CaCu}_2\text{O}_8$ takes one third the time that the LAPW method takes.

2.3 Implementing the Projector Basis Method

This section presents the major details of implementing the projector basis method. First, the local basis functions are discussed. Finally, the iterative eigenvalue solve is described.

Details of the Local Basis

The functions used as the local basis should provide a good representation of the true wave function inside the MT sphere. Inside the muffin tin, the wave function for a crystalline solid should more closely resemble atomic wave functions as the center is approached, because the effects of the rest of the crystal are shielded by the core electrons. Thus, a natural choice for local functions would be functions similar to atomic orbitals.

In general, the local functions should mimic the atomic orbitals in both energy value and angular momentum character. However, the local functions are not limited to those of isolated atomic systems. For example, for a given element, a spread of energies for a certain l may be desired to give the wave function more variational freedom. Since the plane waves penetrate into the MT sphere and are not orthogonal to the inner core orbitals, pseudopotentials are used to remove these inner core orbitals. However, if it is known that high lying core orbitals affect the valence states, a hard pseudopotential can be generated which includes these electrons—hard pseudopotentials do not present any difficulty.

To define a local orbital with angular momentum character l , one starts with the

solution of the atomic-like Schrödinger equation

$$(-\nabla^2 + V^{l=0} + V_{pseud}^l - \epsilon)u = 0. \quad (2.27)$$

Here $V^{l=0}$ is the $l = 0$ part of the total potential, and V_{pseud}^l is the l th component of the nonlocal pseudopotential (see, for example, Figure 1.1). The orbital is calculated for a specific energy ϵ , which is typically at the center of a band with that angular momentum character. In practice, this equation is solved semi-relativistically, which means that the equivalent Dirac equation is solved, but only for the “large” solution. The resulting local orbitals may be recalculated on every self-consistent iteration, or they may be frozen for the entire calculation.

The one requirement on the local orbitals is that they vanish on the muffin tin surface. As defined in (2.27), the local orbitals do not, implying that the local orbitals have tails in all of the neighboring MT spheres. In order to enforce this requirement, a set of Gaussian functions is subtracted from the local orbitals,

$$\tilde{u}(r) = u'(r) - (x_1 + x_2 e^{-(a_2 r)^2} + x_3 e^{-(a_3 r)^2}). \quad (2.28)$$

The Gaussians are chosen so that the first two derivatives of \tilde{u} vanish at the MT surface. The addition of the Gaussians to the basis functions adds additional correction terms to the Hamiltonian. However, this does not present a problem as the Gaussian functions, and hence the added terms, are easily expanded in plane waves.

The Eigenvalue Solver

The implementation of the eigenvalue solver is a very crucial part of an electronic structure code. As discussed earlier (see Eq. 2.18), the general matrix form of the eigenvalue equation to be solved is

$$H\Psi = \epsilon S\Psi, \quad (2.29)$$

where S is the overlap matrix and ψ is the vector of basis function coefficients. Since the dimension of this matrix is equal to the number of basis functions, it can be solved exactly only for very small systems. Plane wave methods generally use a steepest descent-type algorithm, such as the conjugate gradient method [2], while other methods may use standard iterative techniques [23] or Cholesky-Householder techniques [24].

The method used here is an iterative procedure proposed by Singh for the LAPW method [25], and is based on the block Davidson method [23]. Unlike many iterative eigenvalue solvers which calculate eigenvalues one at a time, the block Davidson method calculates the m smallest eigenvalues simultaneously, where m is much smaller than the size of the matrix. One advantage of this method is the eigenvectors will not converge to incorrect eigenvectors as can happen in other iterative methods [23]. In addition, degenerate states are not a problem.

The interpretation given to m in electronic structure calculations is that each of the m eigenvalues and its corresponding eigenvector represents a band. Hence, if there are one hundred electrons in the current problem, then only fifty doubly occupied bands are needed to hold them. Hence, even though there may be five hundred to one thousand basis functions, the size of the matrix diagonalized is much smaller. However, the value used for m is generally at least twice the number of bands needed, so that there will be enough variational freedom to correctly find all of the needed bands.

The block Davidson method, as with most iterative eigenvalue solvers, is based on using the residual R to update the current eigenvector,

$$\delta R(\Psi) = (H - \epsilon S)\Psi \quad (2.30)$$

$$\Psi_{new} = \Psi - (H - \epsilon S)^{-1}\delta R(\Psi). \quad (2.31)$$

Here, the Ψ are the eigenvectors of the m lowest bands and ϵ is the current approximation

of the eigenvalue. Instead of computing the inverse of $H - \epsilon S$, the diagonal approximation is used as an approximate inverse, i.e. the diagonal elements dominate the matrix, so the matrix inverse is replaced with a matrix containing the reciprocal of the diagonal elements.

Since this method of solution is iterative, a starting guess must be given for the eigenvalues. For the first (self-consistent) iteration, the guess is simply one plane wave for each band. For all subsequent iterations, both within the eigenvalue driver and subsequent self-consistent iterations, the guess used is the eigenvalues/eigenvectors from the previous iteration. Once this smaller (block Davidson) band matrix is created, it is diagonalized following the standard Cholesky-Householder procedure.

It should be noted that the block Davidson procedure is not iterated to convergence within one self-consistent iteration. Generally, three iterations are used for each k point. While this is only sufficient for mRyd accuracy in the eigenvalues, any time spent calculating a solution with higher accuracy would be wasted, as the charge density is not the final charge density and so will change when the preparations for the next self-consistent iteration are made. As the charge density distribution converges, the self-consistent iterations hopefully change the charge density less and less, so that the eigenvalue iterations begin to build on the convergence of previous self-consistent iterations, eventually giving the accuracy needed. The result is that the eigenvalues converge only as fast as the charge density converges, implying that no time is wasted getting exact eigenvalue and eigenvectors before they have any physical meaning.

Chapter 3

Test Calculations

Since the projector basis method is a new method, not only is it necessary to show that the method works and gives acceptable results, there is also a need to show the method's strengths and weaknesses. To this end, this chapter presents sets of calculations on three relatively simple systems, along with one additional complex system.

The first set of calculations is on gallium arsenide. Gallium arsenide is an ideal system for demonstrating the properties of the basis functions used in the projector basis method. The initial system is simple enough that it is easy to do plane wave-only calculations, but the pseudopotentials can also be made hard enough so that calculations require either a large numbers of plane waves or a moderate number of plane waves and a full local basis to achieve a reasonable accuracy. Thus a wide range of basis sets can be compared for efficiency.

The next calculation to be discussed is that of carbon in the diamond structure. Since carbon is a first row element, computation by plane waves can be difficult, while for other methods this is a relatively simple system. It is shown that this system is also a simple system for the projector basis method.

Copper metal, besides being a transition metal, is the source of much interesting physics in materials such as the high- T_c cuprate superconductors, and is the next calculation considered. Here, it will be shown that the projector basis method correctly represents the d -band manifold of FCC copper using both a small and large FFT meshes.

The final calculation performed is a calculation of the normal state of the bismuth high- T_C superconductor $\text{Bi}_2\text{Sr}_2\text{Ca}_1\text{Cu}_2\text{O}_8$. Though the tetragonal unit cell has only fifteen atoms, it is a very difficult system to calculate. This system demonstrates how the projector basis method scales to larger systems.

3.1 GaAs

Gallium arsenide was a very popular material on which to do calculations about a decade ago. Since it is used extensively by the semiconductor industry, a large amount of experimental work has been done to determine its properties, and a correspondingly large theoretical effort was undertaken to help explain and understand the experimental results [26]. Hence, there is a large body of results to compare with.

Gallium arsenide exists in the zinc-blende structure with a lattice constant of 5.65\AA . The zinc-blende structure is a face-centered-cubic lattice with two atoms per unit cell. The gallium atom sits on the corners of the cube while the arsenic atom is on the body diagonal half way to the center of the cube.

The pseudopotentials used for gallium and arsenic are both Kerker-style non-local pseudopotentials. To emphasize the robustness of the projector basis method, two very different sets of pseudopotentials are compared. The angular momentum character, cut-off radii, and occupations for each level of the sets are summarized in Table 3.1. In the first set, a more traditional set of valence pseudopotentials is shown. For each atom, pseudopotentials are created for the atomic $4s$ and $4p$ levels, completely removing the core electrons.

Table 3.1: Atomic characters, cut-off radii and occupancies of the different pseudopotentials used in the GaAs calculations.

Valence-like Potential				Core-like Potential		
Atom	Orbital	r_c	Occup.	Orbital	r_c	Occup.
Ga	4s	1.79	1.5	3s	0.55	2.0
	4p	2.08	1.0	3p	0.55	6.0
	4d	2.12	0.5	3d	0.50	10.0
As	4s	1.63	2.0	3s	0.51	2.0
	4p	1.92	2.5	3p	0.51	6.0
	4d	2.12	0.5	3d	0.46	10.0

With this configuration, there are 8 electrons in the unit cell. As indicated by the table, the pseudopotentials can be made for arbitrary electronic configurations. Here, instead of having two electrons in the Ga 4p level, half an electron is placed into the 4d level. It is found that this gives more variational freedom to the basis.

In the second set of potentials, relativistic pseudopotentials are created for the $n = 3$ shell, where the 4s and 4p states are ionized. Now, instead of relying on the pseudopotential to completely represent the core, the calculation has explicit core states that can be relaxed into the crystalline environment. For many systems, such as GaAs, this has no effect on the valence electrons—the core levels are too deep to be affected by the crystalline environment. For other atoms, such as copper or bismuth, these core (or semi-core) levels are close enough to the Fermi energy (within a few eV) that their effects must be included. With this pseudopotential, there are 44 electrons in the calculation.

There are several different ways of using these ionic pseudopotentials. In the first method, the extra charge is evenly rescaled into the pseudopotential during its generation, so that the atoms appear to be neutral. In the second method, the pseudo-atoms are left ionic, so that the mixed basis code can decide how to put the charge back in. The mixed basis code can then rescale the charge either on the atomic sites or in the interstitial.

Table 3.2: Theoretical and experimental results for the eigenvalue spectrum of GaAs at some special k points. All values are in eV.

	PB	PBC	WNR	WSR	WK	FC	CKAE	LPMKS
Γ_{1v}	-12.51	-12.99	-12.45	-12.80	-12.35	-12.33	-13.10	-13.80
Γ_{15}	0.00	0.00	0.00	0.00	0.00	0.00	0.00	0.00
Γ_{1c}	0.95	0.29	0.91	0.26	1.21	1.10		
Γ_{15c}	3.61	3.61	3.61	3.61	3.78			
X_{1v}	-10.02	-10.38	-9.94	-10.37	-9.79	-9.88	-10.75	-10.70
X_{3v}	-6.79	-7.05	-6.74	-6.94	-6.60	-6.62	-6.70	-7.10
X_{5v}	-2.76	-2.80	-2.69	-2.69	-2.64	-2.61	-2.80	-2.50
X_{1c}	1.30	1.17	1.30	1.24	1.61	1.51		
X_{3c}	1.60	1.43	1.57	1.48	1.88			
L_{1v}	-10.80	-11.14	-10.71	-11.11	-10.56	-10.64	-11.24	-12.00
L_{1v}	-6.66	-6.89	-6.59	-6.74	-6.49	-6.46	-6.70	-7.10
L_{3v}	-1.18	-1.19	-1.10	-1.11	-1.12	-1.11	-1.30	-1.40
L_{1c}	1.12	0.77	1.12	0.79	1.37	1.30		
L_{3c}	4.56	4.52	4.51	4.54	5.15			

Currently, the charge is put in the interstitial, so that it can relax back into the atoms. This should give a better charge density for modeling interstitial charge localizations, such as atomic bonding and electriles, which will be discussed in Chapter 5.

The self-consistent eigenvalue spectrum for each of the pseudopotentials is shown in Table 3.2, along with some experimental and theoretical results. The labels are as follows: PBC and PB are the projector basis method, with and without core pseudopotentials, respectively, WNR and WSR are non-relativistic and semi-relativistic all-electron LAPW calculations from Wei [3], WK is the linear combination of Gaussian orbitals calculation of Wang and Klein [27], and FC is a plane wave calculation using Kerker-style pseudopotentials from Froyen and Cohen [28]. The experimental results are angle-resolved photoemission data from Chiang *et al* [29](CKAE) and X-ray photoelectron spectroscopy data from Ley *et al* [30](LPMKS). The eigenvalues from the calculations are in excellent agreement with

both the theoretical and experimental sets of results. It should be noted that the mixed basis method compares well with the semi-relativistic (i.e. large solution of Dirac's equation only) LAPW results, but not with the non-relativistic results. This is due to the fact that, while the mixed basis code is not fully relativistic, it uses a semi-relativistic solution to the radial wave equation for the local orbitals, and pseudopotentials which are generated relativistically.

The details of the mixed basis calculations are as follows. In the PB calculation, the muffin tin radii are 2.15 a.u., and the FFT mesh is $32 \times 32 \times 32$, with a plane wave cutoff energy ($|\vec{k} + \vec{G}|^2$) of 12.2 Ryd for PB, i.e. $RK_{max} = 7.5$. The potentials are expanded up to $l = 8$. With this FFT mesh, the plane waves are fitted by projector functions up to $l = 8$, which yields about 165 projector functions fit over 555 FFT points. In the PBC calculation, the muffin tin radii are 1.25, the plane wave cutoff energy is 31.4 Ryd ($RK_{max} = 7.0$). Using the same FFT mesh as the PB calculation yields 215 FFT points in the MT sphere, and the fitting is done up to $l = 6$, using 85 projector functions. It should be noted that, in both of these calculations, the plane wave cutoff energy is above that needed for a reasonable convergence.

To explore how the mixed basis code behaves with different combinations of local orbitals, GaAs was calculated, using the core pseudopotentials, for 5 different basis sets. Table 3.3 details the local part of each different basis set. Set 1, which is identical to the calculation above, contains orbitals with energies corresponding to the $n = 3$ core shell and the $n = 4$ valence shell for both the Ga and As atoms, while Set 3 contains only the $n = 3$ shell levels. In the second set, the Ga has only the $n = 3$ core levels, while the As has both the $n = 3$ and $n = 4$ levels. It should be noted that the fourth set uses the mixed basis code as a hard pseudopotential plane wave code. The final set contains the $3d$ levels and the $n = 4$ levels.

Table 3.3: Energy parameters and sizes of the different basis sets used to explore how the local basis affects the calculated eigenvalues, in Ryd.

	Set 1		Set 2		Set 3		Set 4		Set 5	
	Ga	As	Ga	As	Ga	As	Ga	As	Ga	As
<i>s</i>	-9.50	-12.50	-9.50	-12.50	-9.50	-12.50			0.20	-0.10
	0.20	-0.10		-0.10						
<i>p</i>	-6.20	-8.70	-6.20	-8.70	-6.20	-8.70			0.40	0.40
	0.40	0.40		0.40						
<i>d</i>	-0.35	-1.90	-0.35	-1.90	-0.35	-1.90			-0.35	-1.90

The results of these calculations are shown in Table 3.4. Between Sets 1 through 3, the largest variation is for the Γ_{1c} band. This valence band is known to be inaccurately calculated by the LDA [3,31], not because of deficiencies in numerical implementations, but due to the inherent inability of the LDA to calculate excited states (it is a theory of the ground state). For the other bands, only a very small change is noted. This is because the plane wave energy cut-off is higher than that needed for a reasonable degree of convergence. Hence the removal of the higher lying orbitals from the spectrum is easily compensated by the plane wave sector. In Set 4, however, it is seen that the plane wave cut-off energy is not sufficient to represent the $n = 3$ bands; the energy pattern of the bands is not recognizable as GaAs bands. The results for the fifth set are very interesting. The upper levels of the spectrum are almost identical to the converged results. The difference is only in the Ga and As $3s$ levels, which are higher by 6.02 and 2.92 eV, respectively; the $3p$ levels are represented correctly by the plane waves. It is interesting to note that, even though the inner core levels are incorrect, the upper core and valence levels are represented correctly. This run was repeated again, but without the $3d$ local orbital, and the results were similar to those of Set 4.

To verify that the shape of the charge is correct, a series of charge density contour plots is shown in Figure 3.1. The plots are made in the $[1\bar{1}0]$ plane, with successive contours

Table 3.4: Comparison of the eigenvalue spectrum of GaAs for different combinations of local basis functions, in eV.

	Set 1	Set 2	Set 3	Set 4	Set 5
Γ_{1v}	-12.99	-12.98	-12.84	-5.64	-12.99
Γ_{15}	0.00	0.00	0.00	0.00	0.00
Γ_{1c}	0.29	0.33	0.59	3.85	0.27
Γ_{15c}	3.61	3.61	3.64	5.15	3.61
X_{1v}	-10.38	-10.38	-10.14	-5.64	-10.39
X_{3v}	-7.05	-7.02	-6.95	-5.12	-7.05
X_{5v}	-2.80	-2.80	-2.78	-3.09	-2.80
X_{1c}	1.17	1.17	1.26	-0.03	1.18
X_{3c}	1.43	1.45	1.48	1.38	1.44
L_{1v}	-11.14	-11.14	-10.92	-27.68	-11.15
L_{1v}	-6.89	-6.87	-6.82	-15.16	-6.89
L_{3v}	-1.19	-1.19	-1.18	-5.89	1.19
L_{1c}	0.77	0.81	0.96	-4.68	0.77
L_{3c}	4.52	4.52	4.54	-4.18	4.53

separated by two electrons/unit cell volume. Panel D shows the valence charge density from the calculation of Wang and Klein [27], and is typical of the charge density plots found in the literature. Panel C shows the valence charge from the converged non-core calculation described above, while Panels A and B show the charge from the core pseudopotential calculation. The difference between Panels A and B is in the number of bands plotted. Panel A shows the full valence charge density for the core calculation, while Panel B shows only the charge density due to the occupied valence bands. As can be seen from Panels B and C, the charge density is fully reproduced.

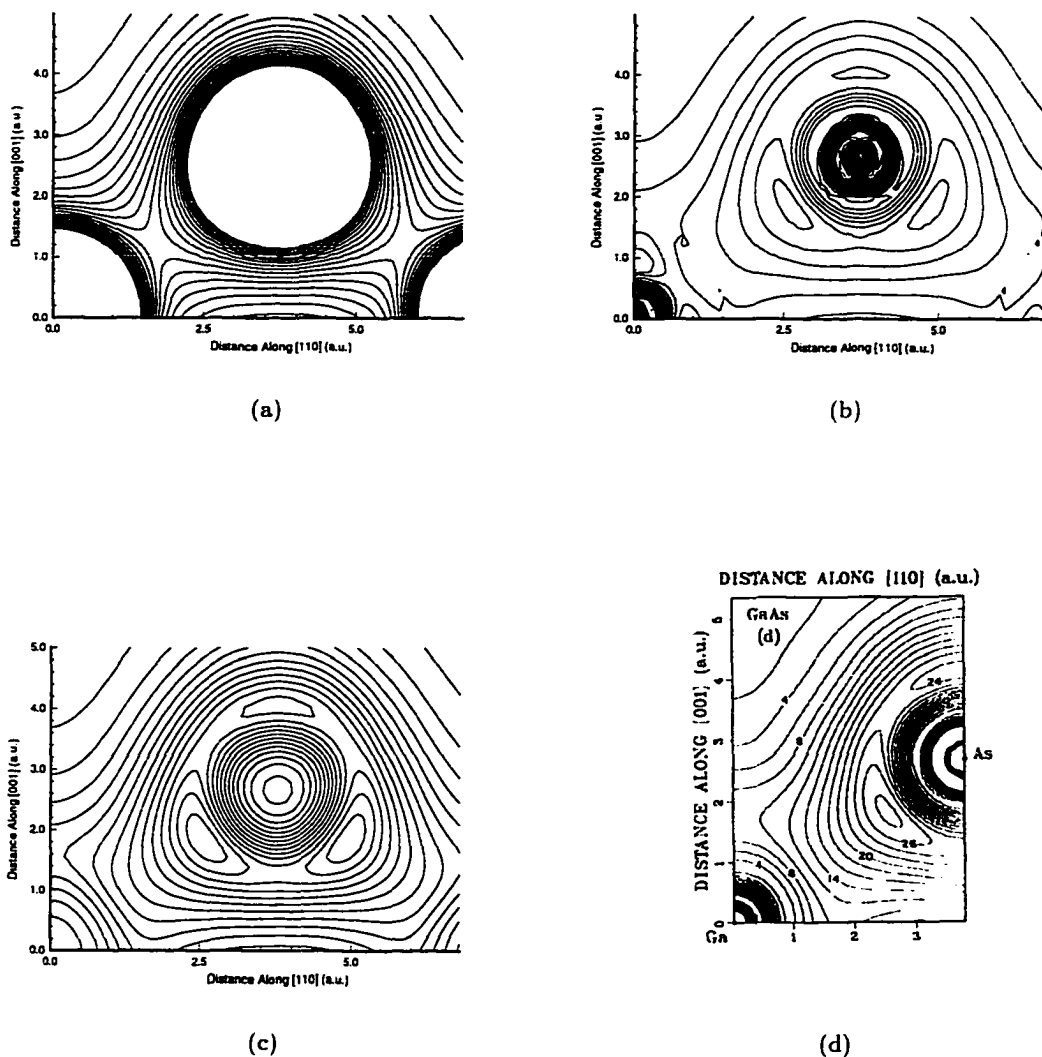


Figure 3.1: Comparison of the GaAs charge densities in the $[1\bar{1}0]$ plane. Panels (a) and (b) correspond to the core pseudopotential calculation. Panel (c) is the non-core pseudopotential calculation and Panel d is the pseudopotential calculation of Wang and Klein [27]. The distance between contours is 2 electrons/unit cell volume in Panels (b), (c) and (d).

3.2 Carbon

While gallium arsenide represented a simple system to calculate, carbon represents difficulties which are similar to the the core potential calculation of gallium arsenide: some of the valence orbitals can be tightly bound. These tightly bound orbitals can give plane wave methods trouble, while MT-based methods have no difficulty calculating them.

The lattice that is used in the calculation here is the same as that used for the gallium arsenide calculation above, the zinc-blende structure. This common form of carbon is also known as diamond, and the structure referred to as the diamond structure. The lattice constant is 6.746 atomic units.

The converged basis set consists of a single s and a single p orbital, with energies of -0.5 and 1.1 eV, respectively. While these are valence orbitals, the shape of the orbitals is such that local orbitals are required. One reason for this is due to the small size of the atoms. A similar valence orbital on a larger atom has more room to spread out, but on a first row element, the orbital is constrained to a smaller region of space, and so has a sharp, peaked structure.

The pseudopotential is created for the $2s$ and $2p$ orbitals, both of which have cut-off radii of 1.15 atomic units. The FFT mesh used is $32 \times 32 \times 32$, which gives 675 FFT points inside the MT sphere of radius 1.45. Using these FFT points, the real space plane wave mesh was fit up to $l = 8$ using 165 projector functions. RK_{max} was taken to be 8.5 ($|\vec{k} + \vec{G}|^2 = 34.4$), which yields about 270 plane waves in the basis. In the eigenvalue solving step, 20 bands were kept initially, and the usual 3 iterations of the block-Davidson method were performed. The calculation converged very quickly, taking only about 10 self-consistent iterations using 2 special k points [32–34]. Special k points are used as the points in a Gaussian quadrature-type scheme for integrations over the entire Brillouin zone.

The results of the calculation are displayed in Table 3.5. The LAPW results are

Table 3.5: Comparison of the theoretical and experimental eigenvalue spectrum for diamond, in eV.

method	PB	LAPW	EPP	PW
Γ_1	-21.44	-21.42	-21.34	-21.38
$\Gamma_{25'}$	0.00	0.00	0.00	0.00
Γ_{15}	5.55	5.56	5.57	5.51
$\Gamma_{2'}$	13.40	13.40	13.56	13.56
X_1	-12.69	-12.68	-12.66	-12.67
X_4	-6.38	-6.37	-6.34	-6.31
X_1	4.75	4.75	4.79	4.64
X_3	16.60	16.68	16.71	16.81
$L_{2'}$	-15.55	-15.54	-15.52	-15.53
L_1	-13.47	-13.46	-13.41	-13.47
L_3	-2.84	-2.84	-2.81	-2.81
L_3	8.44	8.45	8.45	8.37
L_1	9.04	9.04	9.07	8.97

unpublished results computed for comparison here using the code of Krakauer and collaborators [18, 35–37]. The data labeled EPP is an LCAO calculation using Gaussian orbitals from Erwin *et al* [38], and PW is a pseudopotential plane wave calculation of Pickett and Louie [39]. As can be seen from the table, the projector basis method agrees very well with the other results. While the agreement with the LAPW calculation is excellent, generally better than 0.01 eV, the agreement with the other data is still good, around 0.1 eV. The high agreement with the LAPW is because both calculations were performed with the same input parameters, such as the FFT mesh, plane wave energy cut-off, and pseudopotentials. Changes in these parameters account for most of the deviations from the results of the other methods. One other possible source of the differences is that the mixed basis and LAPW results were only converged at 2 special k points in the irreducible wedge of the Brillouin zone. While this is in general enough points to give good results for semiconductors, the

other calculations used a larger number of k points. The EPP results, for example, are from a 10 k point calculations

To verify that the charge density is reasonable, Figure 3.2 shows the density of states for both the LAPW and mixed basis runs. All of the features of the DOS are represented correctly in the mixed basis run. This demonstrates that the charge is correctly distributed over the energy spectrum.

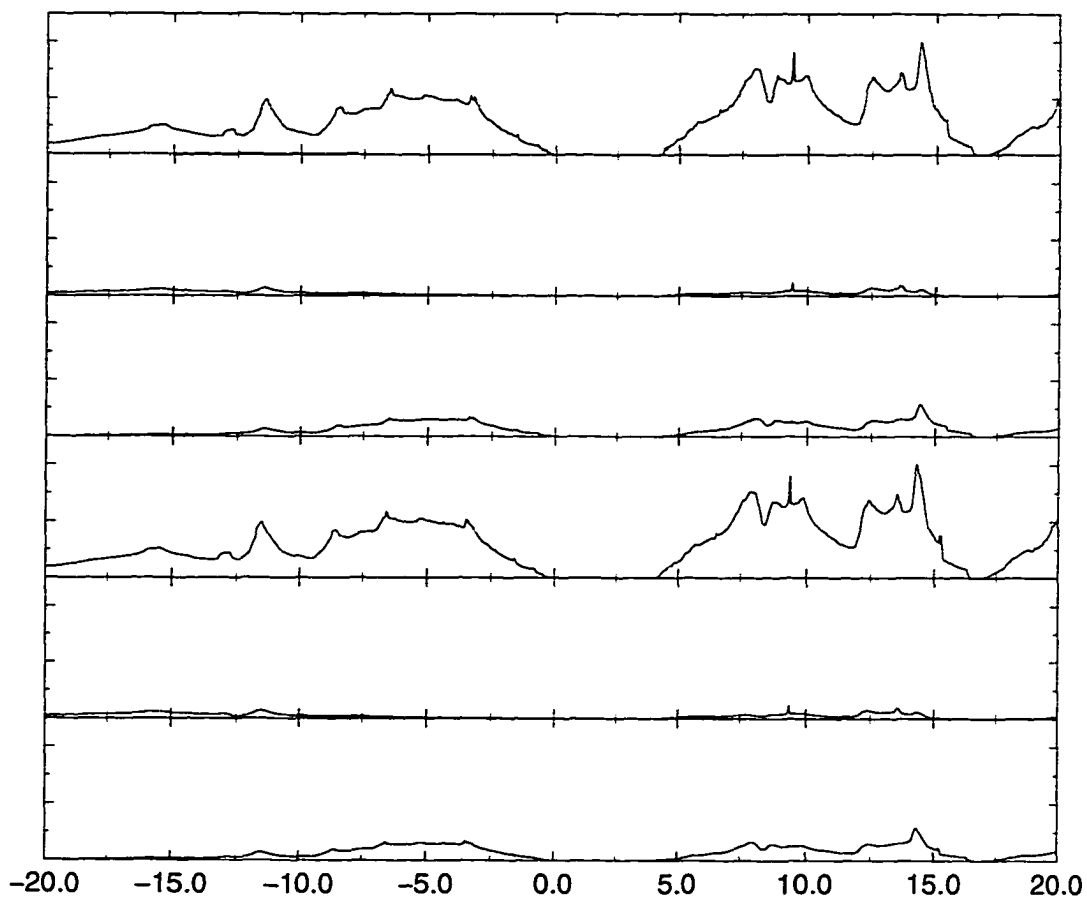


Figure 3.2: Comparison of the DOS for diamond. The top three panels are the total, s , and p projected DOS for an LAPW calculation and the bottom three panels are the corresponding plots for the mixed basis code. The reference energy is the Fermi energy, and the energies are in eV.

3.3 Copper

The next test system for the projector basis method is copper, transition metal system. The electronic structure of copper, like all the transition metals, is dominated by partially filled d bands near the Fermi energy. These bands allow copper to display a wide range of configurations. In copper metal, the $3d$ bands are filled and the $4s$ bands are the source of the conduction electrons. In the high- T_c superconductors, it is thought that the $4s$ bands are filled, leaving holes in the $3d$ bands [40].

The neutral electronic configuration for atomic copper is $3d^{10}4s^1$. The pseudopotentials were calculated for the configuration $3d^{10}4s^{0.8}4p^{0.2}$, with cut-off radii of 0.25, 1.49 and 1.49 a.u., respectively. The $4p$ level is included because the current implementation does not allow for the angular momentum character of the pseudopotential to skip any values of l . The $3d$ is very hard, so that it can represent the true $3d$ potential as accurately as possible. The $4s$ and $4p$ potentials, on the other hand, are relatively soft.

Metallic copper exists in an FCC structure with a lattice parameter of 6.822 atomic units. The local basis consists of single p and d orbitals, each with energy 0.4 Ryd. The s orbital is easily represented by plane waves, due to the softness of the potentials and the fact that the plane wave cut-off energy is rather high, 20.0 Ryd ($RK_{max} = 8.5$). The only reason a p orbital is needed to correctly describe some of the higher p -like conduction bands, such as $X_{4'}$ and $L_{2'}$.

To demonstrate that the projector basis method behaves well with a large FFT mesh, the calculation for copper was done for two different mesh sizes. The first, PB1, is $20 \times 20 \times 20$ and the second, PB2, is $28 \times 28 \times 28$. The results from these calculations, along with other theoretical results, are displayed in Table 3.6. It is obvious that PB1 is well converged with respect to PB2, with differences generally less than 2 mRyd. The only eigenvalue that shows a greater difference is Γ_{15} . The obvious problem with a larger FFT

Table 3.6: Comparison of theoretical eigenvalue spectrums for fcc copper, in Rydbergs.

	PB1	PB2	MJW	P	LAPW
Γ_1	-0.513	-0.513	-0.515	-0.517	-0.515
$\Gamma_{25'}$	-0.062	-0.060	-0.061	-0.057	-0.060
Γ_{12}	0.000	0.000	0.000	0.000	0.000
Γ_{15}	1.909	1.883		2.015	1.927
X_1	-0.196	-0.196	-0.210	-0.197	-0.195
X_3	-0.165	-0.163	-0.167	-0.155	-0.163
X_2	0.042	0.041	0.043	0.039	0.041
X_5	0.053	0.055	0.058	0.053	0.054
$X_{4'}$	0.282	0.282	0.297	0.300	0.287
X_1	0.702	0.701		0.680	0.700
$X_{5'}$	1.121	1.122		1.138	1.126
L_1	-0.210	-0.209	0.209	-0.202	-0.209
L_3	-0.064	-0.063	0.065	-0.061	-0.063
L_3	0.042	0.043	0.046	0.042	0.043
$L_{2'}$	0.098	0.098	0.093	0.103	0.103
L_1	0.453	0.453		0.441	0.448
$L_{3'}$	1.690	1.689		1.797	1.708

mesh is that the calculation is significantly slower. However, the biggest problem with a large FFT mesh is the possibility that the plane waves will be able to fit the same features that the local basis fits, causing either the convergence to stall as charge sloshes between the two representations, or the eigenvalues are incorrect.

The differences at Γ_{15} between the two mixed basis runs appear to be due to the quality of the projector basis fit to the plane waves. While testing the convergence of copper, one basis set used consisted of only a single d orbital at 0.4. Using this basis, the p -like bands at $X_{4'}$, $X_{5'}$, $L_{2'}$, and $L_{3'}$ displayed errors of up to 150 mRyd compared to the other theoretical values, but the p -like Γ_{15} band only had an error of about 4 mRyd. This behavior was consistent for both of the FFT meshes. Adding the single p orbital gives the results in the table.

The only difference between the two calculations is the FFT mesh. In PB1, there are 369 FFT points in the MT sphere, and the fitting is done using 120 projector functions, up to $l = 7$. In PB2, there are 959 points, fit by 165 projector functions, up to $l = 8$. In addition to fitting to a higher l , the PB2 mesh should do a better job fitting the projector functions to the plane waves because the fit is done at a greater number of points. The end result is that the plane waves alone do a good job of fitting the p -like band at Γ_{15} . When the p orbital is added, the plane waves adjust correctly to include the local orbital. However, if the plane wave cut-off energy is increased much higher than the plane waves should compete with the local orbital, causing catastrophic errors in the calculation.

The remaining data in Table 3.6 are theoretical. The LAPW calculation is again an unpublished calculation designed to match PB2. The MJW data are a non-relativistic KKR calculation [41, 42] from Moruzzi, Janak and Williams [43]. The calculation labeled P is an APW calculation from Papaconstantopoulos [44]. In general, the results are very good, with the differences from PB1 and PB2 less than a few mRyd.

The final value for Γ_{15} , however, is still different from that of the other calculations. It should be noted that the validity of the LAPW results high in the conduction band may be questionable. The energy parameters for the LAPW basis functions are set around the Fermi energy, and may not be good choices for bands that are 1.5 Ryd away. A trial run on the LAPW code with the p energy parameters at 1.9 Ryd showed the Γ_{15} eigenvalue drop by close to 0.1 Ryd. While the LAPW was not converged using this basis, this does indicate that the high conduction band eigenvalues are not necessarily correct.

In Figure 3.3, the band structure of copper is displayed along several of the high symmetry directions. This picture was generated from the results of a second calculation on the $28 \times 28 \times 28$ mesh. This second calculation utilized a set of 19 special k points, while the original utilized a set of 2 special k points. It should be noted that, while the

eigenvalues at the original set of k points is unchanged, the band structure at the general set of k points is changed dramatically. The main difference is that band crossings calculated as anti-crossings. It should be noted that it is a known fact that calculations for metals need a larger number of k points to accurately describe the partially filled band that crosses the Fermi level. The plot was generated from the converged charge density by explicitly calculating the eigenvalue spectrum at 150 points along four high symmetry lines.

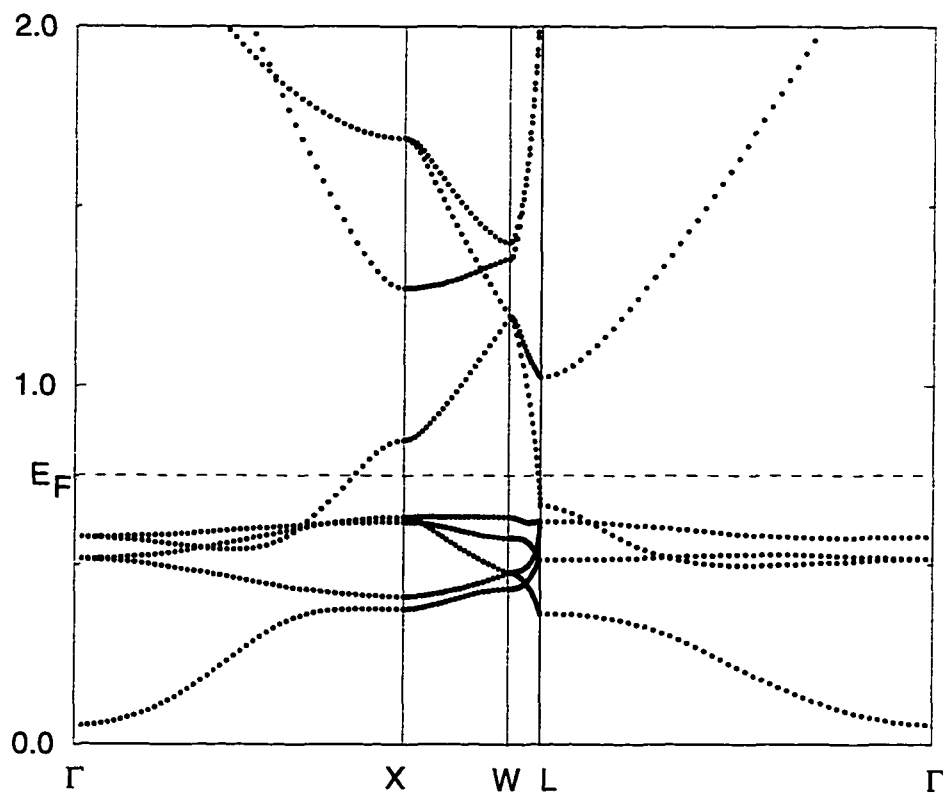


Figure 3.3: Energy bands for fcc copper along selected high-symmetry directions, in Ryd. The dashed line represents the Fermi energy.

3.4 $\text{Bi}_2\text{Sr}_2\text{Ca}_1\text{Cu}_2\text{O}_8$

The final calculation for this chapter is on one of the bismuth high- T_C materials. $\text{Bi}_2\text{Sr}_2\text{Ca}_1\text{Cu}_2\text{O}_8$ (BSCCO) was discovered to be a high- T_C superconductor by Maeda *et al* [45] in 1988. While the crystalline properties of BSCCO (stability, easy cleavage at known crystalline planes) allowed for an intense experimental study, the complex crystalline structure made detailed theoretical studies very difficult to perform. The actual structure [46–48] is a four formula unit orthorhombic cell with an incommensurate modulation of $0.21b^*$, giving a unit cell with a volume of about 30,000 a.u.³ and about 300 atoms. However, it was found that the first order structure, a single formula unit tetragonal cell [49,50], was computationally tractable.

First principles LAPW calculations have been performed by Massidda *et al* [51], Hybertsen and Mattheiss [52], Krakauer and Pickett [53] and Sterne and Wang [54]. These calculations predict and explain much of the BSCCO system, but have differences from the experimental picture. For example, the small piece of the Fermi surface at \bar{M} (see Figure 3.5) is suggested to be a flat band just below the Fermi energy [40,55]. This and several other differences are believed to be due to strong electron-electron correlations by some [40], while calculations by Singh and Pickett [56] suggest that calculation's use of the first order structure could be the cause.

The structure of the tetragonal unit cell was given by Tarascon *et al* [49] and by Sunshine *et al* [50] in 1988. The structure, as show in Figure 3.4, consists of dual Cu-O perovskite-like layers alternating with dual Bi-O sheets. For the following calculation, the structure from Tarascon is used. The space group is $I4/mmm$ with $a = 3.814 \text{ \AA}$ and $c = 30.52 \text{ \AA}$.

The details of the local basis are described in Table 3.7. The basis is a very minimalistic one; the softer details of the charge are left to the plane waves. The bismuth

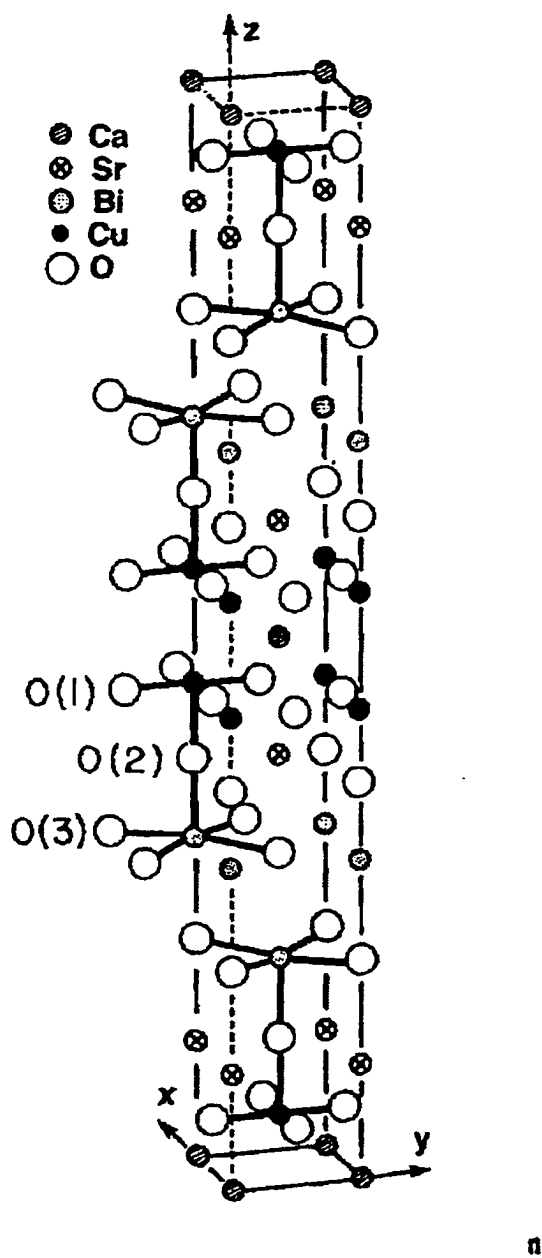


Figure 3.4: Unit cell of BSCCO, from [49].

Table 3.7: Energy parameters and sizes of the basis set used in the calculation of BSCCO, in Ryd.

	<i>s</i>	<i>p</i>	<i>d</i>
Bi			
Sr			
Ca	-2.20		
Cu			0.70
O	-0.84	0.15	

and strontium atoms have pseudopotentials created for the 6*s* and 6*p*, and the 5*s* levels, respectively. The calcium atom is also has a pseudopotential created for the 3*s* level, but this level is such that it is too difficult for the plane wave basis to represent, so a local orbital is added. The copper potential is similar to that of the previous section, but here is represented by a single *d* orbital. Finally, the oxygen has pseudopotentials created for the 2*s* and 2*p* levels. With these details, there are 43 local functions. It should be noted that, with these pseudopotentials, the calculation is very sensitive to the addition of certain types of basis functions. For example, adding a local Sr *s* function at -1.8 Ryd or a Ca *p* function at -1.0 Ryd causes spurious eigenvalues to ruin the calculation. The cause appears to be linear dependence with the plane wave sector, even though these levels are rather deep. One indication of this is that the states have a large weight in the interstitial region (55% and 40%, respectively).

The FFT mesh is $32 \times 32 \times 128$. This, combined with a plane wave cut-off energy of 25 Ryd, yields 3170 plane waves in the basis. With the pseudopotentials given above, there are 110 electrons, and so the eigenvalue solver keeps 100 bands. With 3 special *k* points, convergence is obtained in about 30 self-consistent iterations. The time for each self-consistent iteration is about 45 minutes on an SGI Power Indigo 2, and about 30 minutes on a single node of an IBM SP2.

The primary focus of most of the current theoretical investigations of BSCCO is the Fermi surface. The Fermi surface in the (001) plane is shown in Figure 3.5, which reproduces that of Krakauer and Pickett [53]. Here, it is seen that there are two barrel-shaped pieces centered on $X(Y)$, with another small tubular-shaped piece at \bar{M} . As indicated above, experiments suggest that the Cu-O bands, which form the tubular piece at \bar{M} , may not cross the Fermi energy, but rather lie just below it. These experiments suggest that the bands around \bar{M} do not have a minimum there, but rather a shallow maximum [40,55]. The LDA bands show a definite minimum in the bands [53]. A second difference some experiments show is with the Bi-O bands that form the barrel-shaped pieces. Some experiments show that the Bi-O are not entirely centered on $X(Y)$, but that one of the barrels is centered on Γ [40]. To account for these differences, most experimentalists use the LDA's one electron approximation. However, even with the one electron approximation, the LDA can still give reasonable charge densities for similar high- T_C systems, such as La_2CuO_4 [57]. In addition, calculations on the full BSCCO structure, with its additional oxygen atoms and structural variations, could be enough to account for the differences [56]. However, this calculation is still beyond the scope of available resources.

Using a local LAPW code, timings against the mixed basis code were made. Using identical dimensions and basis sets, it was found that, for one self-consistent iteration, the mixed basis code was approximately 30 percent faster than the LAPW code. Since these codes share significant amounts of code (including the heart of the iterative eigenvalue driver), this speed difference can be attributed to differences in how the block Davidson matrix (the matrix of bands) is generated. This supports the supposition that the break even point for speed between the mixed basis and LAPW codes is at 8 to 10 atoms.

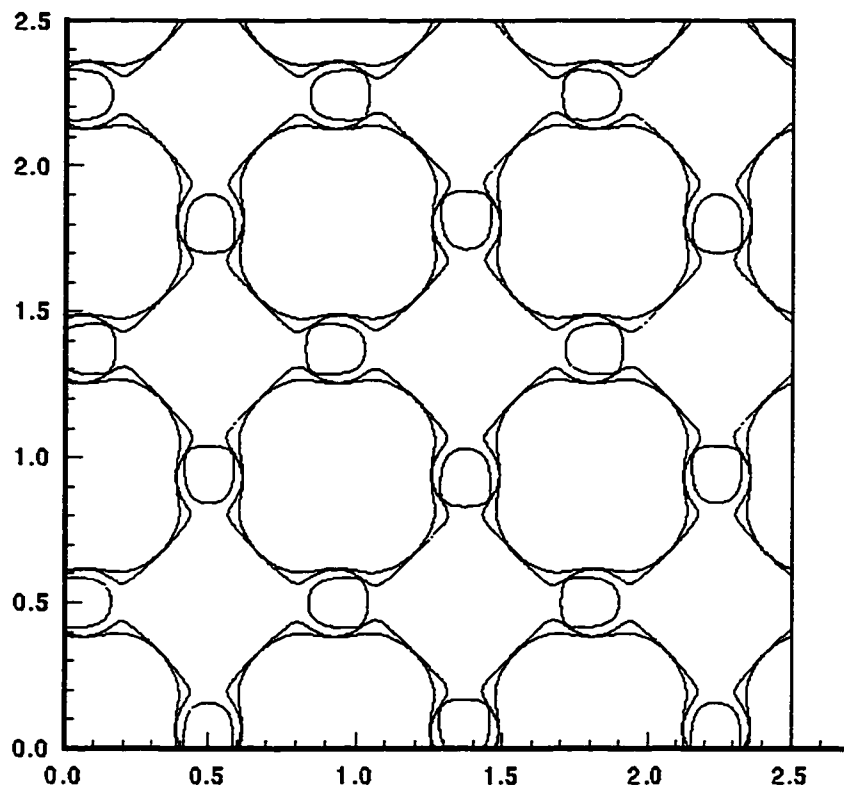


Figure 3.5: Fermi surface of BSCCO calculated in the (001) direction at the plane $z = 0$. Γ is located at $(0,0)$, X is at $(1,0)$ and \bar{M} is at $(0.5,0)$. Units of lattice parameters.

Chapter 4

Electrides

4.1 Introduction

Electrides form a novel class of ionic solids in which the anion is not an atom, but rather an electron trapped or localized in the region of space where the anion is normally located. These novel materials are interesting not only because of this unusual structure, but also because of the wide variety of properties different electrides can exhibit. In one type of electride, the crown ethers, the localized electrons interact very weakly [58], while in the cryptands, the electrons strongly overlap and have an almost metallic behavior [59].

Electrides were first hypothesized to exist in 1956 by Peierls [60] and later by Overhauser [61], as periodic arrays of color centers. A color center is point defect in which an anion is missing, with an electron bound to the anionic site to preserve charge neutrality. The relationship between color centers and electrides will be discussed more fully below.

The existence of electrides was established while studying alkalide solutions [62–64]. Alkalides are solutions of the form Ma^+Mb^- [62, 65], where Ma and Mb are alkali metal cations and anions, respectively. Alkalides exist because the alkali atoms have higher

electropositivity (lower ionization potential) than all of the other atomic families. This allows them to be both the cation (by losing an electron) and the anion (by gaining an electron). Normally, only the cation form is seen, but it is possible to see the anionic phase under standard conditions [66,67]. It was found that adding a complexant, Cx, to the solution greatly enhanced the stability of the anionic phase, and hence the creation of alkalides, now of the form $Ma^+C_xMb^-$. The role of the complexant is to separate the cation and anion, thus keeping them from reacting. These types of materials led the way to the synthesis of electrides.

The work on alkalide solutions began in 1974, and even then included by-products that contained regions with electride-like properties. However, the solutions containing electrides were very unstable, and it was several years before stabilizing solvents were found [62]. Even then, it was not until 1983 that good crystalline samples of electrides were made [59,62]. The crystals proved to be extremely reactive, irreversibly decomposing in minutes when exposed to air. In general, the crystals must be kept in a vacuum and below -50°C .

While good crystalline samples were available in 1983, details of the structure were not known until 1986 when Dawes *et al* [68] published the structure of the cesium crown ether electrides. The cesium crown ether electrides was shown to consist of a cesium atom confined to a cage formed by a sandwich of two crown ether molecules (see Figure 4.1). The trapped electron was assumed to reside in the cavity between adjacent crowns. The structure of the second major class of electrides, the cryptands, was not available until much later. The structure of the lithium cryptands, for example, was made available in preprint form in early 1995 [69]. In these electrides, the cation is trapped inside a football-shaped cryptand molecule (see Figure 4.5, with the anionic electrons presumably in interstitial regions between the cryptands [70]).

Depending on the complexant, a typical cage molecule of an electride can contain 45 or more atoms, and a unit cell can contain one or more cages. Due to the large number of atoms in the unit cell, the only calculations previously available on these materials have been limited to a single complexant or a single complexant and a cation [71–76]. Using the projector basis method, Singh *et al* were the first to do a full *ab initio* calculation of a crystalline electride [77], a cesium crown ether, which will be discussed more fully below. A second calculation, on the lithium cryptand, is presented here.

As indicated above, the idea of electrons substituting for anions is not new. In point defects, the electron is bound in a weak potential well created by the absence of an isolated anion [78]. In an electride, however, the bound electrons lie at *all* of the negative ion sites in the crystalline lattice, where the nature of the forces binding the electrons to the lattice site is substantially different. As will be shown below, the anionic site is in a large region where the potential is a strong plateau, as opposed to a potential well. The electron lowers its kinetic energy by spreading out over the volume of the anionic site, and is thus bound to the site. The anion site in electrides can be large, 2.5 Å or greater in diameter, while a typical color center site is about the size of an atom, ~ 1 Å.

Electrides display a wide range of physical properties. In the cesium crown ethers, the anionic electrons are almost completely localized, with very little interaction between the sites. At temperatures higher than 10 K, these materials are paramagnetic, but at lower temperatures, they become antiferromagnetic [63]. This effect is not seen in the rubidium- and potassium-based crown ethers. In cryptands, on the other hand, the electrons interact more strongly [63]. The Li-2.1.1 compound is paramagnetic, with the paramagnetism approaching zero at 0 K. This temperature dependent spin pairing is due to some of the electrons being close enough to interact in pairs, but at high temperatures thermal energy can break apart the pairs, causing them to exhibit Curie-Weiss behavior [63, 79]. In K-2.2.2,

on the other hand, the electrical and optical behavior is metallic [63,80]. The electrons have the characteristics of a solid containing weakly bound electron pairs: a small paramagnetism which increases slightly with temperature.

The remainder of this chapter is organized as follows. The next section describes a calculation of the Cs based crown ether Cs-(15-crown-5), and the final section describes the cryptand Li-2.1.1. Both of these calculations are extremely difficult, and cannot be done by conventional electronic structure methods. Instead, the mixed basis method described in Chapter 2 is used.

4.2 Cs⁺(15-crown-5)₂·e⁻

The first *ab initio* calculation on an electride [77] was done on the first class of electrides synthesized, the crown ethers [59]. The complexant, a crown ether, $n(\text{CH}_2\text{CH}_2\text{O}) \equiv (3n\text{-crown-}n)$, resembles a crown, as shown in Figure 4.1. The base of the crown is a ring of oxygen atoms, the second layer is a ring of carbon atoms, and the points of the crown are hydrogen atoms. The electride considered here, Cs⁺(15-crown-5)₂·e⁻, is a sandwich of two crown ether molecules surrounding a cesium atom. The Cs electride crystallizes in a triclinic $P\bar{1}$ structure with $a = 8.597$, $b = 8.886$ and $c = 9.941$ Å, $\alpha = 102.91^\circ$, $\beta = 90.06^\circ$, and $\gamma = 97.74^\circ$ [81]. The unit cell of the electride consists of two anti-parallel crown ether molecules sandwiching an alkali atom, and contains 71 atoms. The crown ethers, which are highly polar molecules [82], are oriented such that the negatively charged oxygen rings are nearest to the alkali atom, as shown in Figure 4.1.

The basis used in this calculation consists of 12219 plane waves, using a kinetic energy cutoff energy of 22.4 Ryd and 187 local basis functions, which are described in Table 4.1. The Cs 5s and 5p states are found to be hybridized and band-like, and so are also included. Local functions were also placed on the H atoms, though it was found later that

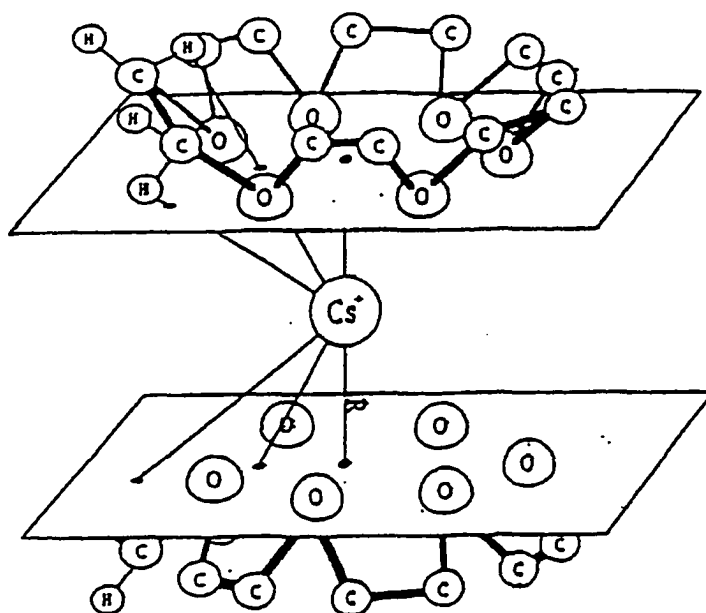


Figure 4.1: Structure of the cesium crown ether, from Dye *et al.*

Table 4.1: Energy parameters for the local orbitals in the crown ether calculation, in Ryd.

	<i>s</i>	<i>p</i>	<i>d</i>
Cs	-1.4	-0.5	-5.0
	-1.0	-0.1	-4.0
	0.5	0.5	0.5
O	-1.1	0.5	
C	-0.8	0.5	
H	0.5		

Table 4.2: Dispersion of the states near E_F for the crown ether electride. E_v is the valence band maximum, E_{elec} is the electride state and E_c is the conduction band minimum. The k -points are given in reciprocal lattice units, the three directions corresponding to the a , b and c axes, respectively.

k -point	Brillouin zone k -dispersions, in eV		
	E_v	E_{elec}	E_c
0,0,0	-0.01	4.48	5.32
1/2,0,0	0.00	4.47	5.20
0,1/2,0	-0.03	4.55	4.98
0,0,1/2	-0.03	4.46	5.13
1/2,1/2,1/2	-0.02	4.61	4.92

they were not needed. The calculation includes 130 electrons, which are described by 100 bands.

The resulting band structure is very complicated, and is shown schematically in Figure 4.2. There is an energy ‘gap’ of ~ 5 eV separating the occupied manifold of bonding molecular orbitals from the unoccupied manifold of anti-bonding molecular orbitals. About 0.4 eV from the top of this gap is a narrow electride energy band of width ~ 0.15 eV, originating from the Cs 6s electron and containing exactly one electron. Table 4.2 shows the dispersion of the states near the Fermi energy. The electride state is highly anisotropic, with the largest dispersion from the zone center occurring along the b axis.

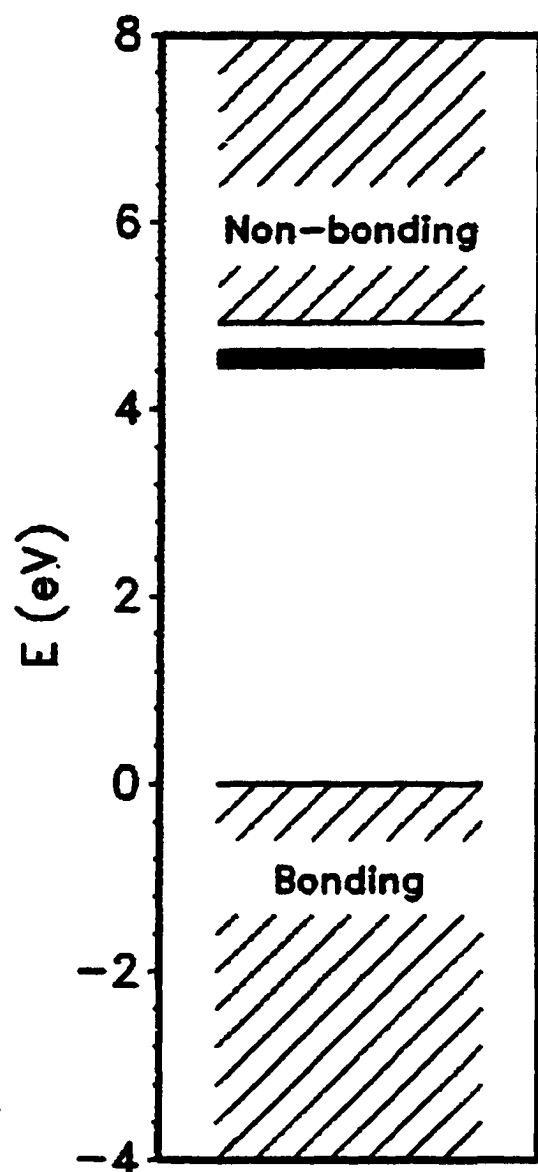


Figure 4.2: Schematic representation of the electronic energy bands for an electride. The top of the bonding bands is the zero of energy for the spectrum. The single band in the gap (represented by the shaded region) can either be half occupied, as in the case of the cesium crown ether, or double occupied, as in the case of the lithium cryptand.

Figure 4.3 shows the charge density of the electrone level as a sequence of constant-density surfaces, corresponding to densities that range from 2.0 to 7.0×10^{-4} e per a.u.³, the average density of a single electron in the unit cell being 2.02×10^{-4} e per a.u.³. This density was obtained from the wave function at Γ , with minor differences seen at the other points in the zone. The volume shown is a cube of edge 24.0 e a.u., ~ 2.8 times the volume of a single unit cell. The charge density of the electrone state is centered in the cavity at $(1/2, 1/2, 1/2)$ and reaches a maximum (9.5×10^{-4}) there. At the highest density in Figure 4.3, the electrone state forms isolated pockets located in the central cavities. The 5.0×10^{-4} e per a.u.³ surface reveals a narrow one-dimensional channel that has opened up along the b axis, connecting the cavity to those in neighboring cells. A narrower channel is also present along the a directions, but none opens up along the c axis. As seen in Table 4.2, the k -space dispersion in the $\langle 1, 0, 0 \rangle$ and $\langle 0, 0, 1 \rangle$ directions is only $\sim 20\%$ of that along $\langle 0, 1, 0 \rangle$, reflecting the greater overlap of the electrone state charge density in the b -axis channel.

Several models have been suggested to explain the mechanism that keeps the electrone states bound and localized in the cavities, where one might expect to find anions. Allan *et al* [65] suggest that the potential in the cavity is a relative minimum so that the electron sits in a well, and Rencsok *et al* [82] suggest that crown ether molecules create a potential 'barrier' that keeps the electron bound. Figure 4.4 shows a plane of the self-consistent potential rendered as a contour plot and as a perspective surface. The plane is nearly parallel to the crystal's ab plane, and passes through the center of the cavity. As can be seen, the potential in the cavity is at a maximum and is not surrounded by potential barrier. One explanation for why the electron remains bound in a region with a repulsive potential is orthogonality. The electrone state must remain orthogonal to the large manifold of bonding molecular orbitals. The electron can thus lower its kinetic energy by avoiding the attractive potentials near the crown ether molecules. Also, the electron can lower its kinetic energy

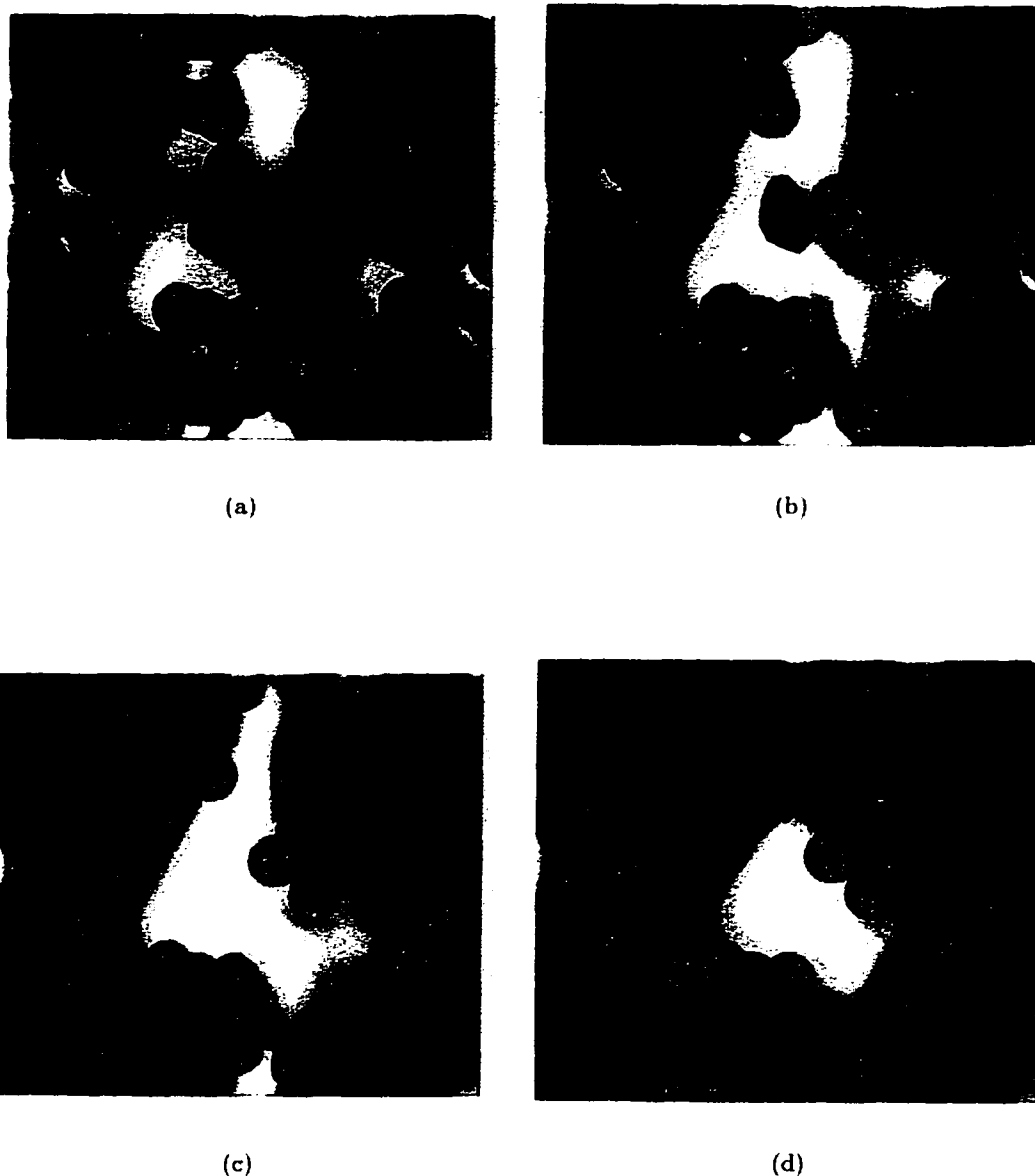


Figure 4.3: The charge density of the electrified state represented by four isosurfaces. The density of (a)-(d) is $2.0, 3.5, 5.0$ and $7.0 \times 10^{-4} \text{ e/a.u.}^3$. The green, red, blue and yellow spheres represent cesium, carbon, oxygen and hydrogen atoms. The A axis is perpendicular to the figure, the b axis is vertical, and the c axis horizontal.

by spreading out over the volume of the spacious cavity. Ultimately, however, the electron remains bound within the solid by the long-range Coulomb tails of the potential.

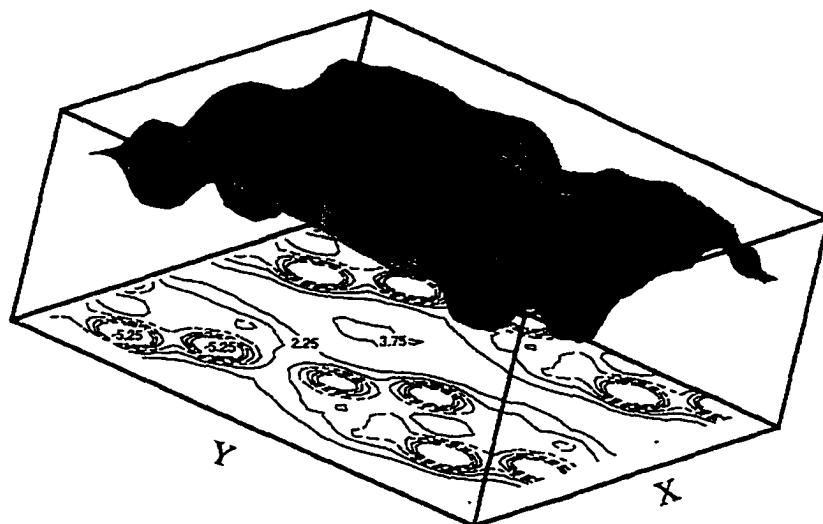


Figure 4.4: The LDA potentials is shown as a perspective surface and contour plot for a plane that cuts through the center of the cavity and is approximately perpendicular to the c axis. The x coincides with the a axis, and the y direction is nearly parallel to the b axis. The contour levels run from -5.25 eV to 3.75 eV in uniform steps of 1.5 eV.

Despite the lack of any formal guarantee, LDA bands are often able to predict whether a material is metallic or insulating. However, when the bands involved are relatively flat, as is the electrider band here, it is found that electron-electron interactions are important. This crown ether electrider is found by optical absorption and d.c. conductivity measurements to be insulating, with a band gap [81] of ~ 1 eV. As the LDA averages over electron-electron interactions, the Hubbard model, with an atomic-like state at each lattice

site, is usually invoked to describe the correlation effects.

In the Hubbard model [78], the band width is represented by $W = 2Zt$, where Z is the number of nearest neighbors and t is the matrix element due to interactions between nearest neighbor states. The energy cost of double occupying the atomic site is U : if the site is singly occupied, then $U = 0$ and the state is a half-filled metallic band. The ratio U/W is then used to characterize the system. If U/W is large, then the system reduces to an antiferromagnetic system with an exchange constant $|J| = 4t^2/U$. In the other limit, U/W is small, the system is a half-filled metallic band. Measured susceptibility measurements near the antiferromagnetic phase transition have extracted values of J between 1.6 and 1.9 K [81]. As the electrone bands are anisotropic (see Table 4.2), the exchange coupling should also be anisotropic. Assuming that the antiferromagnetic transition is dominated by the smallest J value, the smallest calculated band width (i.e., along the a -axis) is used to extract $t_{small} = W_{small}/4$ and $U = 0.15$ eV, using $J = 1.8$ K. A Mott-Hubbard transition occurs when a material ceases to be a conductor and becomes an insulator. An estimate for the transition is given by the ratio U/W_{large} , which yields a value of ~ 1 , using $W_{large} = 0.15$ eV. Given the large anisotropy of the band structure and the half filling of the electrone band, the size of U/W_{large} may result in an insulating state within the Hubbard model.

Given that the LDA averages over the many-body effects which are the heart of the Hubbard model, the results given here are still consistent with the Hubbard model. In the Hubbard model, the electrone state is split into an occupied lower state and an upper unoccupied state. As the optical gap and the estimate of U are much smaller than the gap between the occupied and unoccupied manifolds, the lower Hubbard state must still be located in the gap, and will have the same interstitial character as calculated within the LDA. That the LDA does well in some systems dominated by many-body processes is surprising, but not unusual, as calculations of La_2CuO_4 [83] show.

4.3 $\text{Li}^{-1}-(\text{crypt-2.1.1})\cdot\text{e}^{-}$

The lithium-2.1.1 electride represents the other major class of electrides, those where the complexant is a cryptand. Cryptands, as their name suggests, are molecules whose structure forms a cage, or crypt. The alkali cation is trapped inside this cage, while the localized electrons are presumably bound in the interstitial region between the vaults. Materials containing cryptand molecules were first synthesized by Jean-Marie Lehn and co-workers at the University of Strasbourg in 1969.

In lithium-2.1.1, the cryptand molecule [69] consists of three organic bars that connect two common end-point nitrogen atoms (see Figure 4.5. One of the bars contains two oxygen atoms, while the other two have one oxygen atom each, giving the naming convention 2.1.1. The chain containing two oxygen atoms has the atomic sequence (neglecting hydrogen atoms) N-C-C-O-C-C-O-C-C-N, while the other two chains have the sequence N-C-C-O-C-C-N. The general shape of the resulting cage resembles a football, with the two short chains forming a flat side. Viewed from the end, down the axis of the football, the chains are spaced approximately 120° apart. The nitrogen atoms lie coplanar with the single-oxygen chain oxygens, while the lithium atom, the cation in the electride compound, resides in the center of the crypt, as shown for the potassium-2.2.2 cryptand in Figure 4.5. The chemical composition of each cryptand molecule is $\text{N}_2\text{O}_4\text{C}_{14}\text{H}_{28}$.

The arrangement of these cryptand molecules in the crystal is as follows. Each unit cell contains four molecules, or 196 atoms, two with the corresponding lithium atoms in the $x = 0$ plane and two in the $x = 0.5$ plane, in units of the lattice parameters. The unit cell is orthorhombic (space group Pbcn) with lattice parameters of (10.06, 23.13, 8.38) Å. In the $x = 0$ plane, the lithium atom positions are $(y, z) = (0.1, 0.75)$ and $(0.9, 0.25)$, while in the $x = 0.5$ plane they are $(0.4, 0.25)$ and $(0.6, 0.75)$. The main axis of each football-shaped molecule is oriented approximately along the x axis. In the two molecules with lithium z

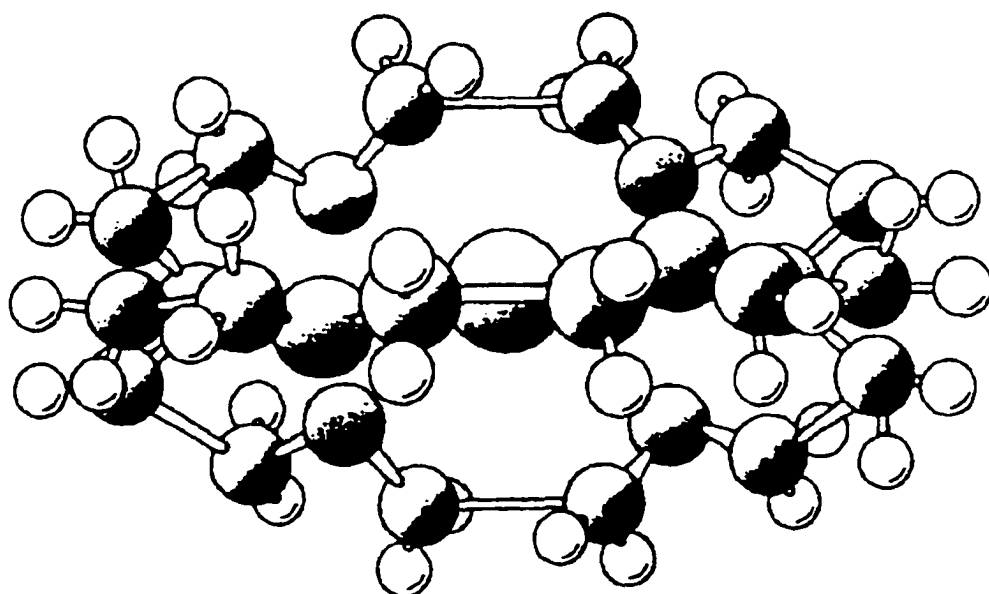


Figure 4.5: Structure of a molecule of the K-2.2.2 cryptand, from [63]. The only structural difference to the Li-2.1.1 is the removal of one oxygen atom and its associated carbons and hydrogens to two of the crypt's chains.

Table 4.3: Energy parameters used in the calculation of Li-crypt-2.1.1, in Ryd. A single local function is placed at each energy.

	<i>s</i>		<i>p</i>	
Li	-2.00	-1.90		
N	-0.40	0.15	0.40	0.60
O	-0.40		0.15	0.25
C	-0.50		0.10	
H				

coordinates of 0.75, the double-oxygen chain is below (in the $x - y$ plane) the molecules, while the single-oxygen chains are above. In the other molecules, the orientation of the chains is reversed.

The details of the local basis are described in Table 4.3. One set of orbitals is used for every atom of a given type, e.g. there would be 8 nitrogen s orbitals. The total number of local orbitals is thus 408. Note that the hydrogen atoms are treated completely by the plane wave sector of the basis. The muffin tin radii of the nitrogen and lithium atoms is 1.32 a.u., 1.25 a.u. for the carbon and oxygen atoms, and 0.465 a.u. for the hydrogen atoms. The plane wave cutoff energy is $|\vec{k} + \vec{G}|^2 = 18.50$ Ryd, which gives 17600 plane waves in the basis. The FFT mesh is $112 \times 220 \times 112$, which gives 250 mesh points in the lithium, nitrogen and oxygen muffin tins, 220 mesh points in the carbon and oxygen spheres, and 12 in the hydrogen spheres. There are 56 projector functions fitting L characters up to 5 for the large atoms, and 4 projector functions fitting up to $l = 1$ for the hydrogen atoms.

The pseudopotentials are again Kerker-style potentials using the Hedin-Lundqvist exchange-correlation potential. The potentials for lithium and hydrogen are as hard as possible: the all-electron potentials are projected into the pseudopotential form. In principle, the cut-off radius can be anywhere, but in practice there are limits on how small it can be. The r_c for hydrogen is made as small as possible, $r_c = 0.02$ a.u., to minimize the effects of

the pseudopotential, while for lithium it is set at 0.34 a.u. Nitrogen, oxygen and carbon have pseudopotentials created for their $2s$ and $2p$ levels. With these potentials, there are 484 electrons left in the system.

In previous calculations, the size of the band matrix was kept at about twice the number of electrons. Since solving the band matrix is the slowest part of a band structure program, much attention was given to trying to minimize both the size of the band matrix and the number of self-consistent iterations needed. Here, it is found that 525 bands gives sufficient accuracy for reliable wave functions and eigenvalues.

To get well converged results took approximately 30 self-consistent iterations at one special k -point, or about 500 hours of CPU time on a single node of an IBM SP2 computer. The large run time allowed good estimates of how the various segments of the code performed. For a run with one k point, the total time used by the code for one self-consistent iteration is 29893 seconds. Of this total, 7005 seconds is spent doing initializations and computing the crystalline potential, 20556 seconds solving eigenvalue problem (3 iterations of the solver), and 2332 seconds is spent computing the charge density and mixing the new and old charge densities. As expected, about 70% of the time is spent solving the eigenvalue equations. Of the time spent on one iteration of the eigenvalue solver, while 2718 seconds is spent computing the FFTs, 1066 seconds computing the band matrix, 224 seconds solving the band matrix, and 2915 seconds computing the wave functions from the band matrix solution. As shown, the actual matrix diagonalization only takes about 3% of the time, while the FFT takes about 40% of the time. This shows that the code scales closer to $O(n^2 \log(n))$ than to $O(n^3)$.

The schematic band structure for the lithium cryptand looks similar to that given in Figure 4.2 for the cesium crown ether in Section 4.2, except that the shaded electrider region contains four bands (instead of only one in the crown ether). To characterize the

band gap anisotropy, some of the k -space dispersions are detailed in Table 4.4. Each of the electrider states is a singly occupied state, as in the cesium cryptand. In the crown ether, the unoccupied (non-bonding or anti-bonding) counterpart of this state was never identified. It resides somewhere in the conduction band manifold, which is a few tenths of an eV above the electrider state. Since there is an odd number of electrons per unit cell, the prediction is that the cesium material is conducting. In this cryptand, the four electrider states are again partially occupied by four electrons, but there is no gap between the lower two bands and the upper two bands. The corresponding anti-bonding bands are again assumed to be somewhere in the conduction band. Since there is an even number of electrons per unit cell, there are three possible behaviors: insulating, semi-metallic or metallic. The Fermi energy (calculated from a single k -point) is $E_F = 3.87$ eV. Thus, for example, the lower electrider states at Γ and X are occupied, but the higher ones are unoccupied. By contrast, all the electrider states are unoccupied at L and $L/2$. This implies that this material is either semi-metallic or metallic. However, evidence of conduction has only been suggested by experimental results. One explanation is that the few studies to date have dealt with either powders or solutions, as large crystals are difficult to grow (unpublished structural information was not even available until mid-1995), and have mainly been concerned with the existence of the localized electrons and their magnetic properties. However, Dawes *et al* [84] describes the conductivity as “reminiscent of near-metallic behavior”. Further evidence for conductivity comes from structural similarity to the much-studied K-2.2.2 cryptand, which is a very strong conductor. Another indication is that the average anionic charge density is larger in the cryptand than in the crown ether. In the lithium cryptand, the average charge density (four electrons/unit-cell) is 3.04×10^{-4} electrons/a.u.³, while in the semiconducting cesium crown ether discussed above it is only 2.0×10^{-4} electrons/a.u.³. As a final note, the dispersion along the $\Gamma - X$ and $\Gamma - Y$ directions is much smaller than

Table 4.4: Brillouin zone k -dispersions at some special k points. E_v represents the valence band maximum, E_{elec} are the values of the electrider levels, and E_c is the value of the conduction band minimum. The extra state above E_c shows the extent of the four-fold degeneracy of the electrider state at $k = L$. The Fermi energy is 3.87 eV.

Brillouin zone k -dispersions					
k -point	E_v	E_{elec}			
$\Gamma, (0,0,0)$	0.00	3.72	3.77	3.81	4.11
$X, (1/2,0,0)$	-0.04	3.74	3.74	3.91	3.91
$(0,1/2,0)$	0.00	3.73	3.73	3.93	3.93
$(0,0,1/2)$	-0.03	3.91	3.91	3.93	3.93
$L, (1/2,1/2,1/2)$	-0.04	3.94	3.94	3.95	3.95
$L/2, (1/4,1/4,1/4)$	-0.02	3.78	3.81	3.90	4.03

along $\Gamma - Z$. This is also reflected in the charge density isosurface plots shown below.

Figures 4.6 through 4.20 show isosurface representations (a single 3d contour) of the anionic charge densities. In each of the figures, the green balls represent the nitrogen atoms and the white balls represent the lithium atoms, with the other atoms left out for clarity. Each side of the displayed rectangular box is ~ 1.3 times the corresponding side of the unit cell. The visualization box thus has a volume of 2.2 unit cells and contains about 430 atoms. The origin of the unit cell is the corner at the lower left, in the back. The red, green and blue axes (labeled x , y and z) correspond to the crystalline a , b and c axes. The surfaces in each figure are isosurfaces of the charge density, and the charge in each surface is that of one or two bands from the given k point. The charge density is constructed by populating all of the states with two electrons.

Figures 4.6 through 4.9 give a sequence of views in the first two, i.e. occupied, bands at $k = \Gamma$. The value at which the isosurface is plotted is 1.5 e/a.u.^3 in the first plot and increases by steps of 0.5 e/a.u.^3 to 3.0 e/a.u.^3 in the final plot. Each isosurface represents one of the electrider bands, so that the integrated charge for each band is two electrons. Recall that the average charge density (two electrons per unit cell) is $1.52 \times 10^{-4} \text{ e/a.u.}^3$. The red

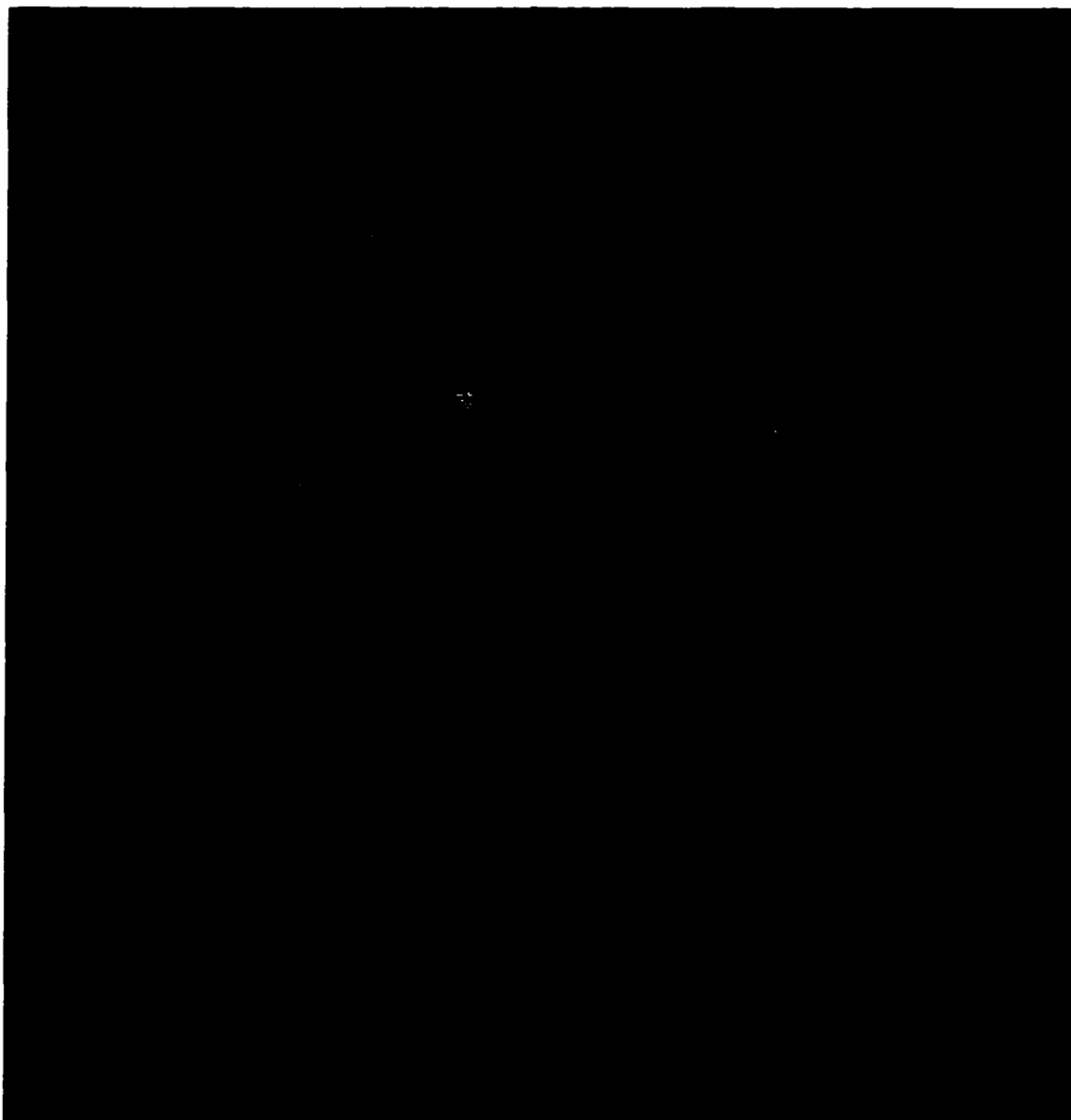


Figure 4.6: This figure, along with the next three, gives a sequence of isosurface plots of the charge density of the first two electride bands, calculated at Γ . The white and green spheres represent the lithium and nitrogen atoms, respectively. The red surface is from the first band, and the yellow the second, and the isosurface value is $1.5 \times 10^{-4} \text{ e/a.u.}^3$.

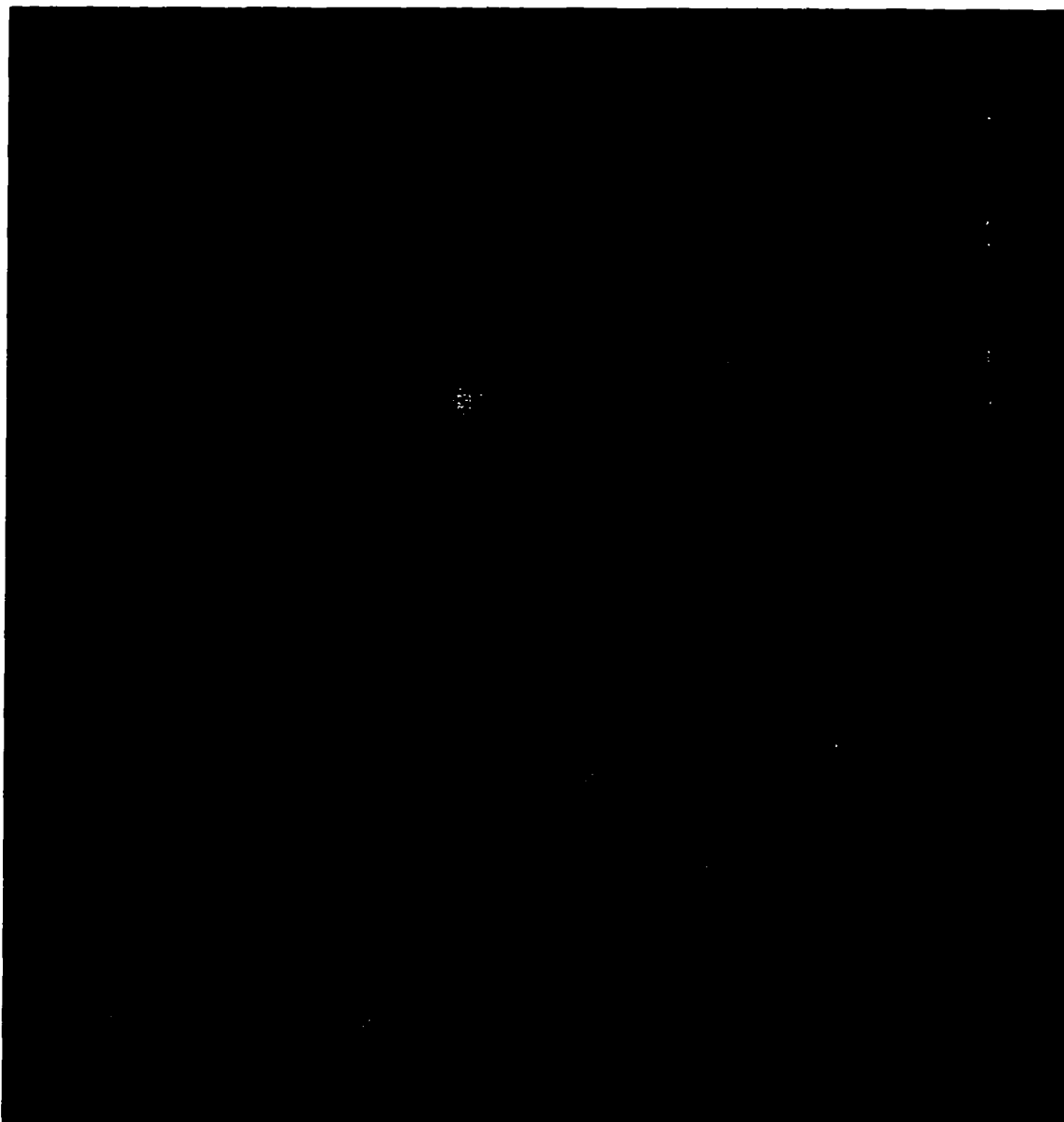


Figure 4.7: An isosurface plot of the electrider bands at Γ , charge density of 2.0×10^{-4} e/a.u.³. See caption for Figure 4.6

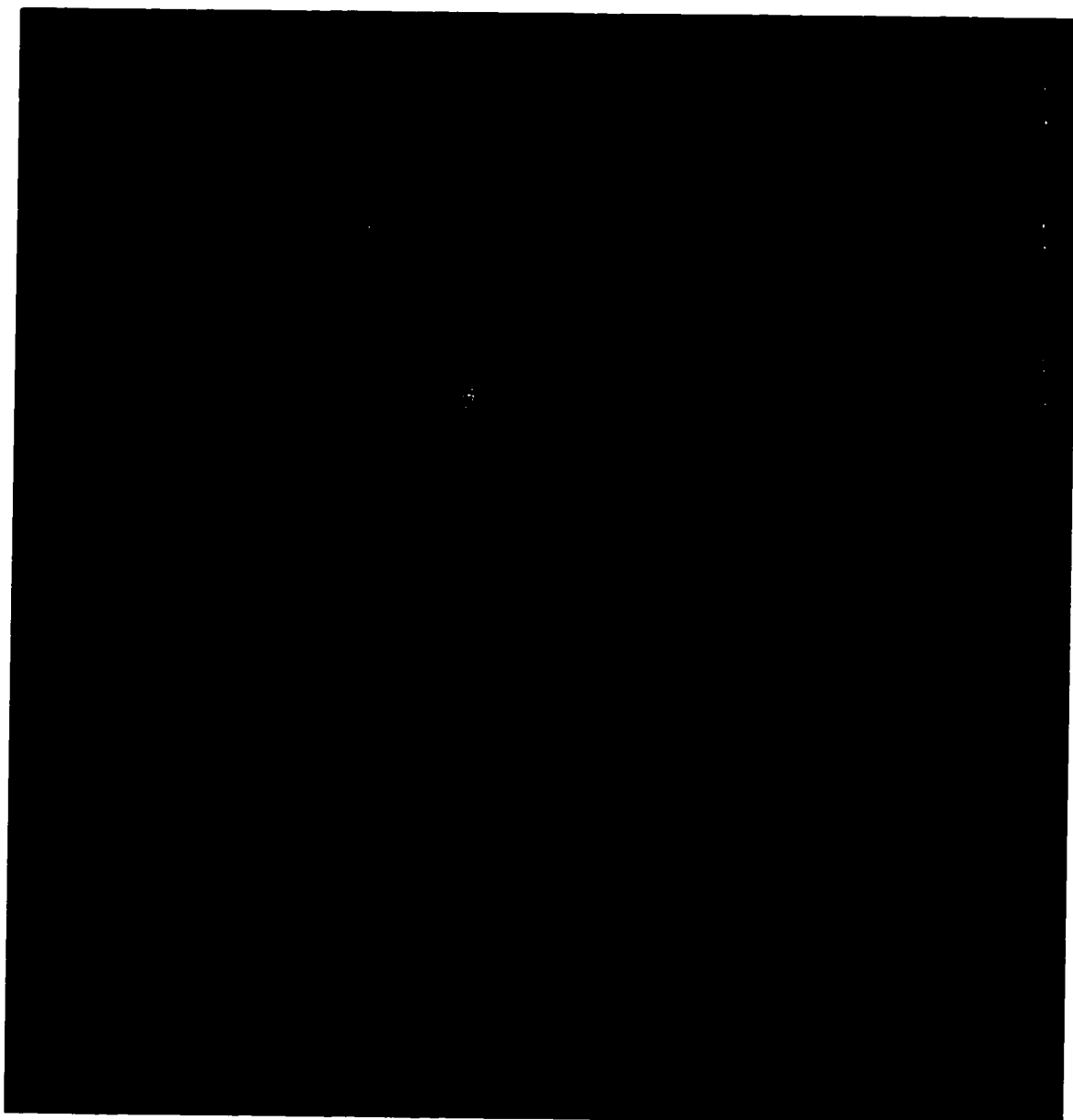


Figure 4.8: An isosurface plot of the electrider bands at Γ , charge density of 2.5×10^{-4} e/a.u.³. See caption for Figure 4.6

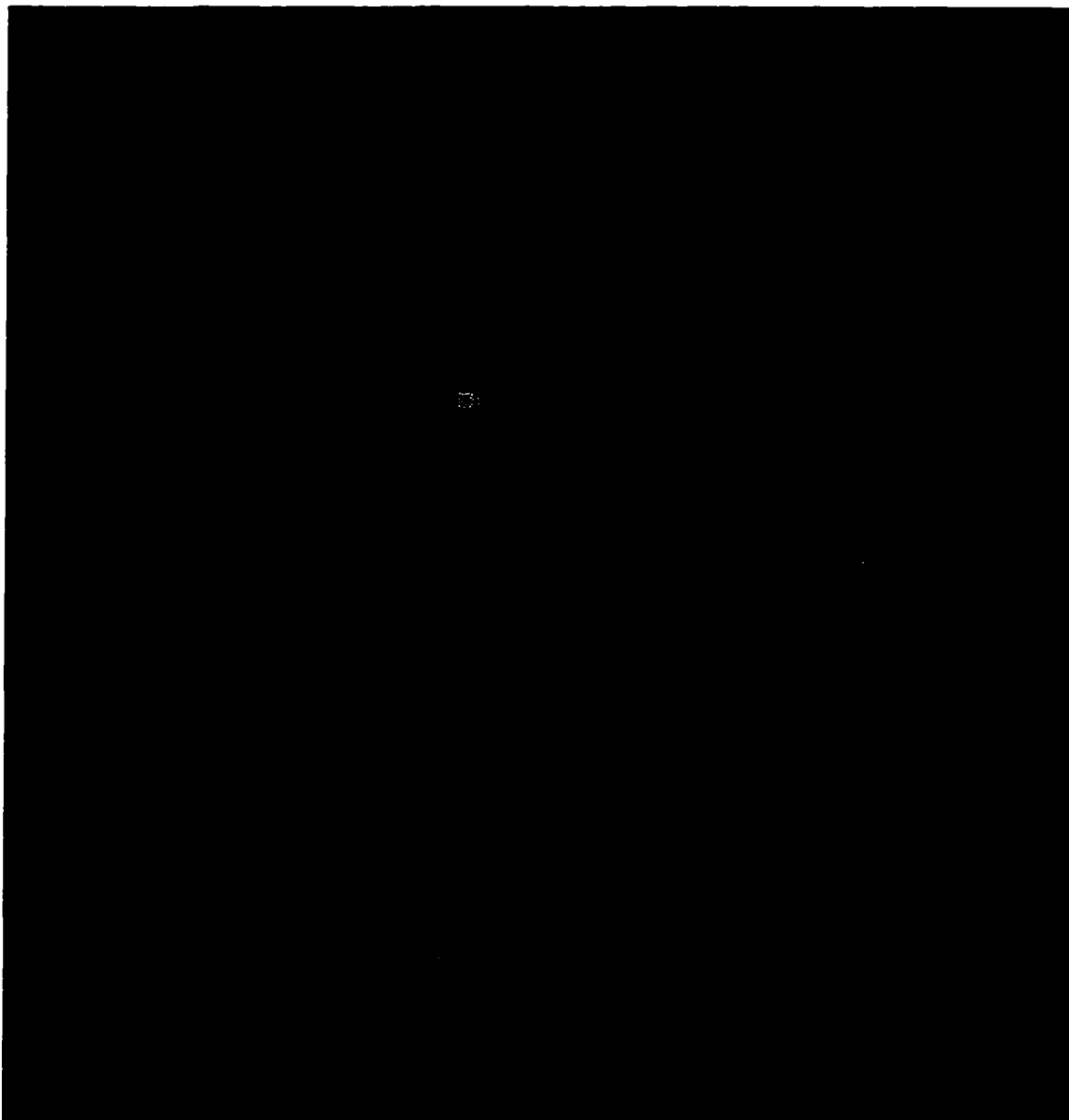


Figure 4.9: An isosurface plot of the electrider bands at Γ , charge density of 3.0×10^{-4} e/a.u.³. See caption for Figure 4.6

surface corresponds to the first electrone band, and the yellow to the second. The charge mostly localizes at the “anionic” sites (the regions between the cryptand molecules), and is shaped like a slightly lopsided elongated dumbbell. The dumbbells are oriented along the y axis. The dumbbell is not located in a region where the potential is symmetric—the end farthest from the lithium atom is smaller and denser than the end nearest. Since there are four anionic sites per unit cell, each dumbbell represents the charge of about one electron.

At the lowest density, Figure 4.6, the two bands are primarily localized in the same region of space. The difference is how the sites are connected: the yellow (upper) band forms channels directed primarily along the y direction between neighboring sites, while the red band forms channels directed along the $y - z$ direction. The isosurfaces for the larger densities show that the yellow surface (the higher energy state, band 2) is somewhat more delocalized at the anionic site than is the red surface (band 1). In addition, the two bands finally localize in different parts of the anionic region, as in Figure 4.8.

Figures 4.10 and 4.11 present a different representation of the occupied electrone states at Γ . The first two bands (plotted as if they contained 4 electrons) are combined in a single isosurface. The value of the density is 2.0×10^{-4} e/a.u.³ in the first figure and 3.0×10^{-4} e/a.u.³ in the second. These figures facilitate comparisons with subsequent figures.

In Figures 4.12 and 4.13, the charge density of the first two bands at Γ is compared with that of the first two electrone bands at L . Recall that all of the electrone states at L are unoccupied. Again, each isosurface contains two bands, or four electrons. The density for each plot is 3.0×10^{-4} and 4.5×10^{-4} e/a.u.³, respectively. In the lower density figure, the localization regions appear to be almost identical. However, the regions from L are not connected while those from Γ are. In the higher density figure, the charge from each surface still localizes in the same region, but the surfaces are shaped somewhat differently

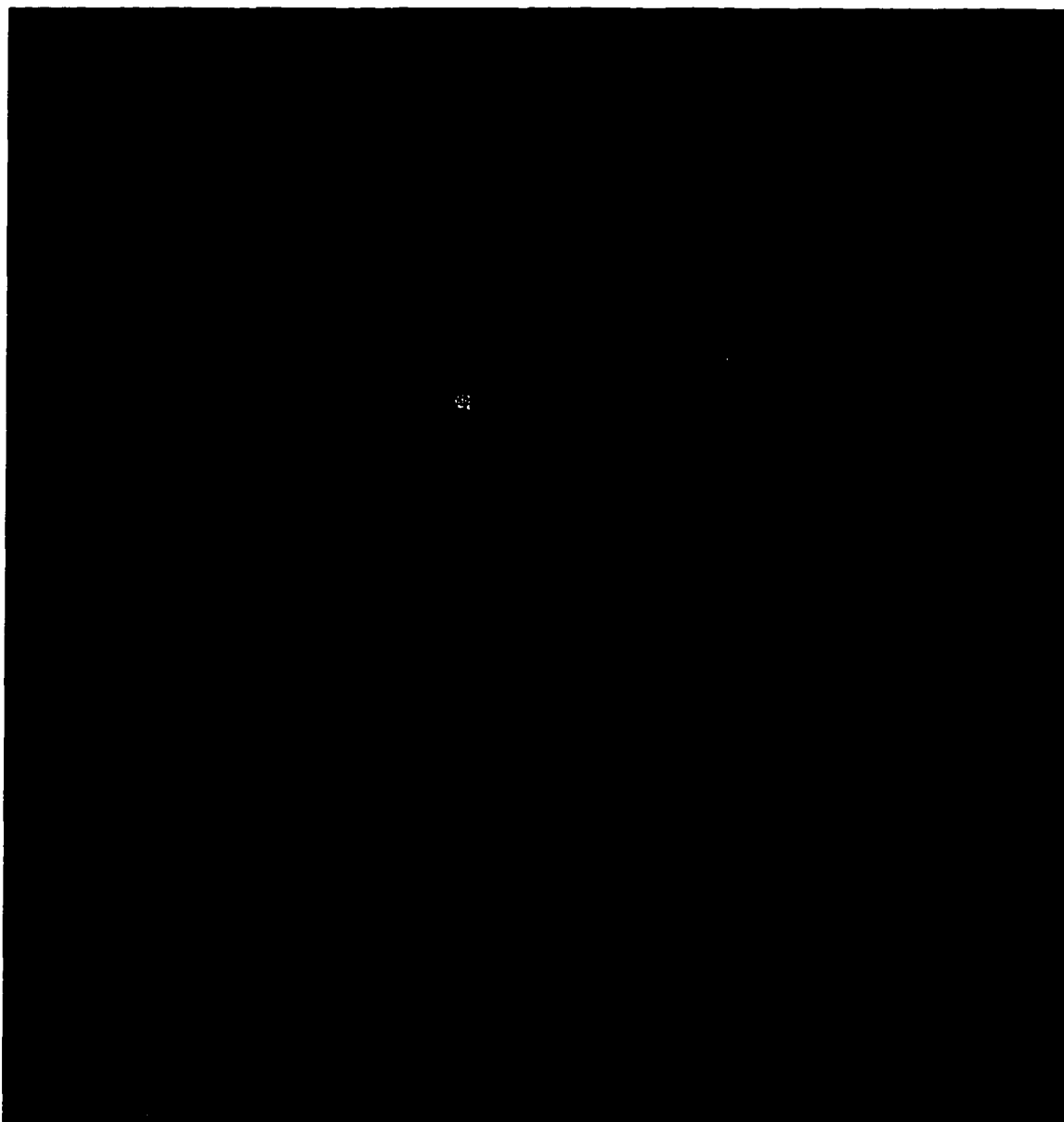


Figure 4.10: The electrone charge density calculated at Γ , but with both bands plotted as a single isosurface. The value of the charge density is $2.0 \times 10^{-4} e/a.u.^3$.

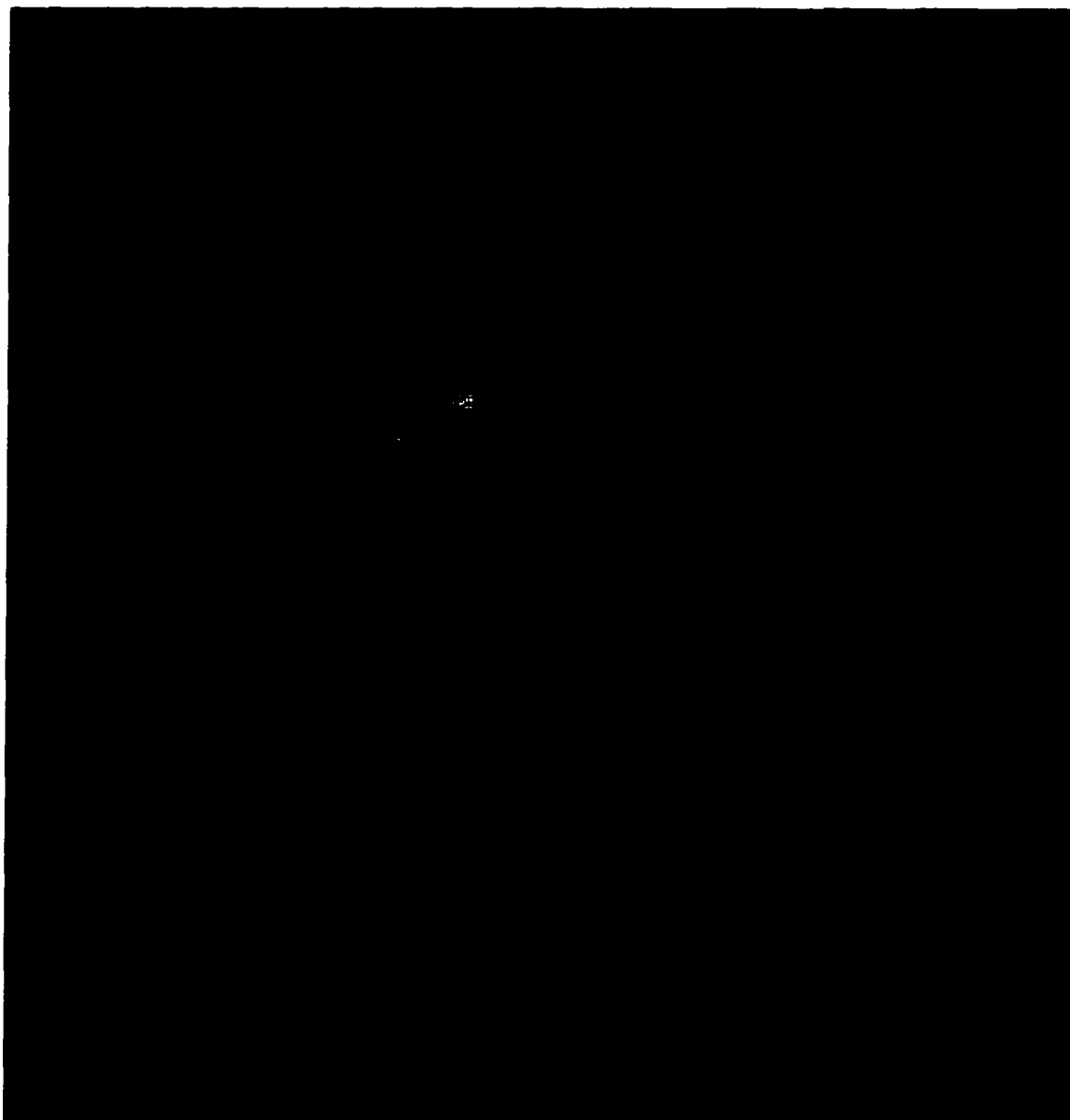


Figure 4.11: Another isosurface of the electrone charge density calculated at Γ , at a charge density value of 3.0×10^{-4} e/a.u.³

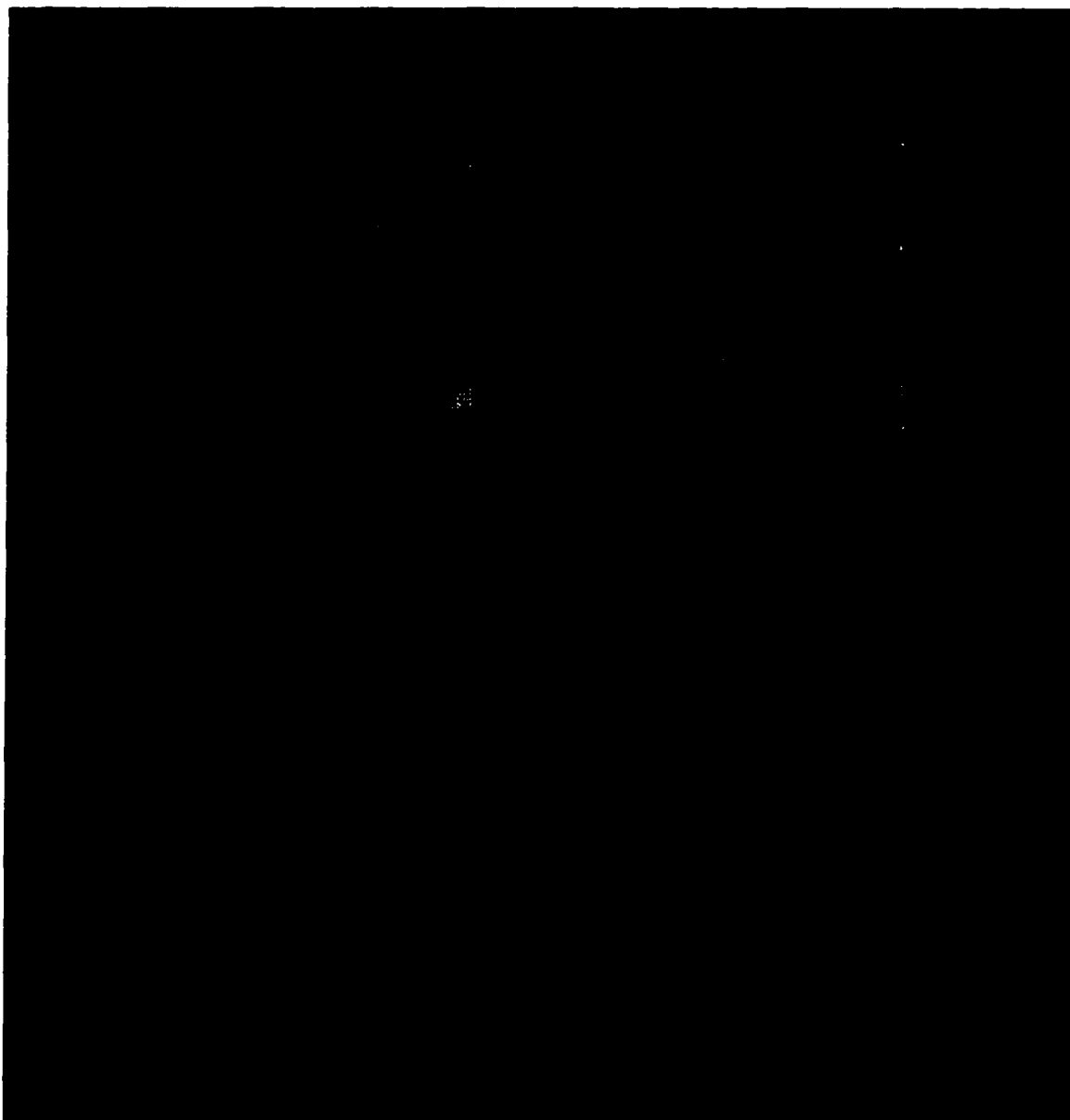


Figure 4.12: This figure and the next compare isosurfaces of the charge densities of the first two bands at Γ (red) and the first two bands at L (yellow). Each surface contains the first two electrone bands. Note that at this density, $3.0 \times 10^{-4} \text{ e/a.u.}^3$, the regions of localization look very similar.

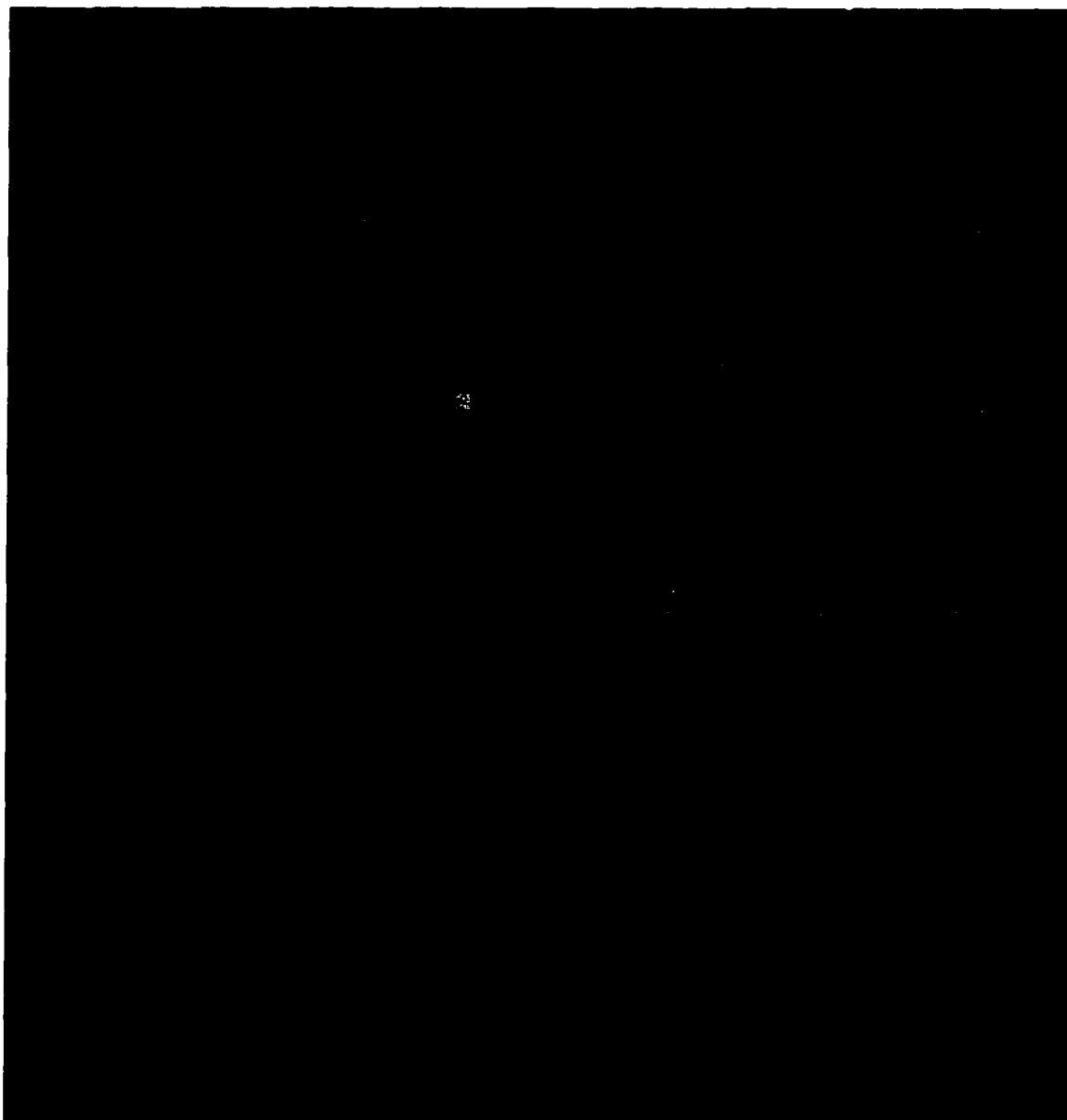


Figure 4.13: A final comparison of the charge density isosurfaces of the first two bands at Γ and L . At a density of 4.5×10^{-4} e/a.u.³, the charge at Γ is still situated in the same region of space as that at L , but encompasses a much smaller volume.

and enclose slightly different volumes. The localization regions at $k = L$ become connected at an isosurface value of $1.5 \times 10^{-4} \text{ e/a.u.}^3$.

Figures 4.14 through 4.16 show a comparison between the first pair electrider bands at Γ with the second pair. The first figure has an isosurface value of $1.5 \times 10^{-4} \text{ e/a.u.}^3$, and shows that the surfaces are essentially the same, with only small differences in the size and shape of the localization region. However, Figure 4.15 shows a significant change. The channels connecting the localization regions for the upper pair of bands (yellow) are completely in the $x - z$ plane, while the lower set of bands are still connected by channels in the $y - z$ direction, the channels are in the $x - z$ plane. The result is that the second pair of bands has a very planar structure, with connections between the different planes occurring at low densities. The final figure, Figure 4.16, shows the surfaces at an isosurface value of $4.5 \times 10^{-4} \text{ e/a.u.}^3$. Here it is seen that the two charge densities are still localized in the same region of space, but channels still connect the localization regions of the upper bands.

The next set of Figures, 4.17 through 4.20, show the potential plotted with several different charge densities. The first figure shows a series of isosurfaces of the potential at a variety of energies. The lower energy plots show the potential shaping itself around the cryptand molecules (the attractive potential near the atoms is large and negative). At higher energies, the potential surface takes on the appearance of a tubular-shaped triangular wave. The potential is seen to attain a maximum (the most repulsive) at the "anionic" sites. In each of the remaining figures, the potential is plotted at a value of 0.45 Ryd (6.1 eV), and each of the charge surfaces contains pairs of bands. When the potential is overlayed with the charge density from Γ (see Figure 4.11), it can be seen that the regions where the charge localizes is in the same regions where the potential most repulsive. Also note that the channels connecting the dumbbell regions primarily follow the shape of the potential. In

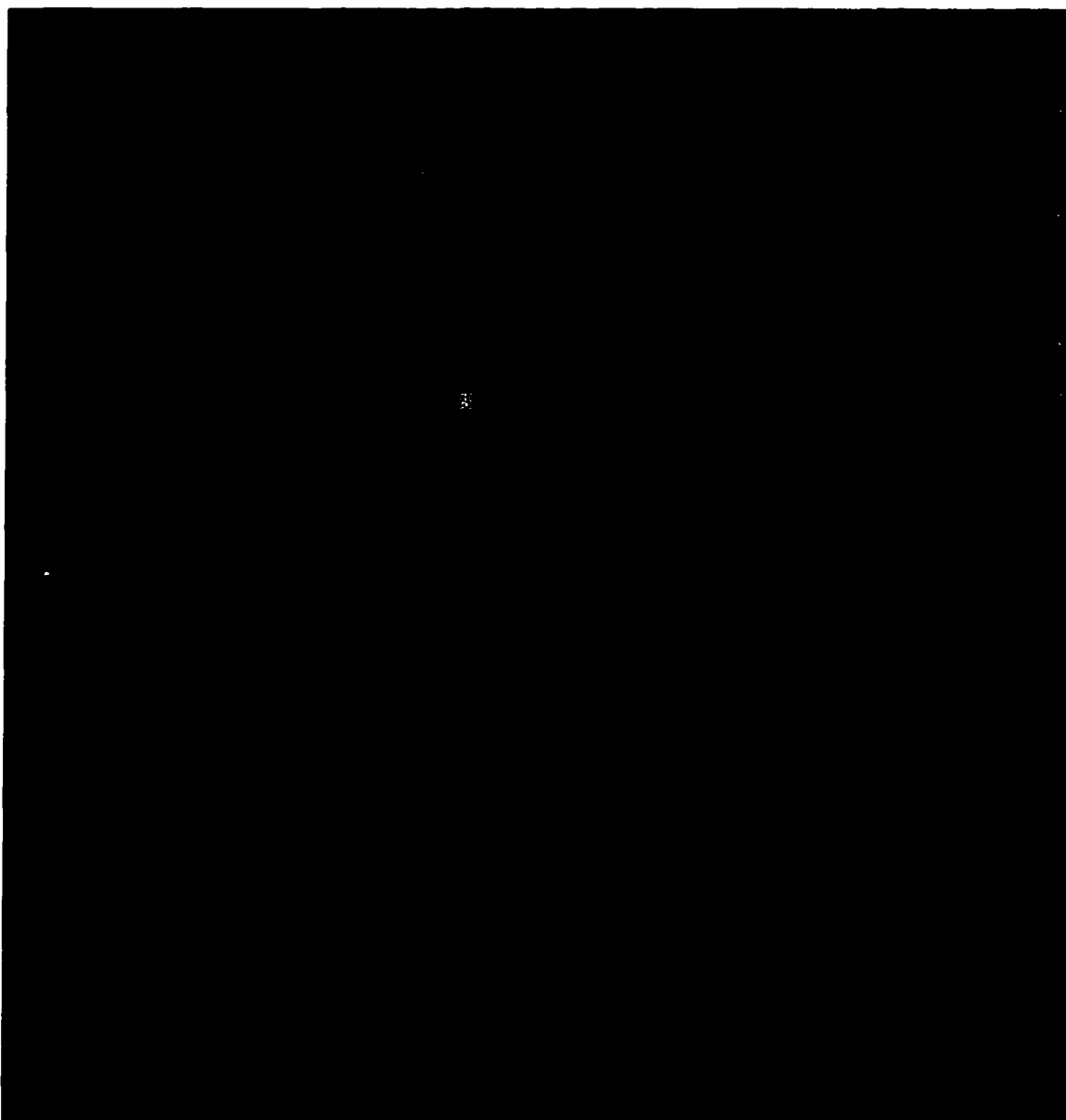


Figure 4.14: This figure, along with and the next two, show isosurfaces of the charge density at Γ . The red band contains the first two electrone bands, while the yellow band contains the second pair. Each surface contains four electrons and has a density of 1.5×10^{-4} e/a.u.³.

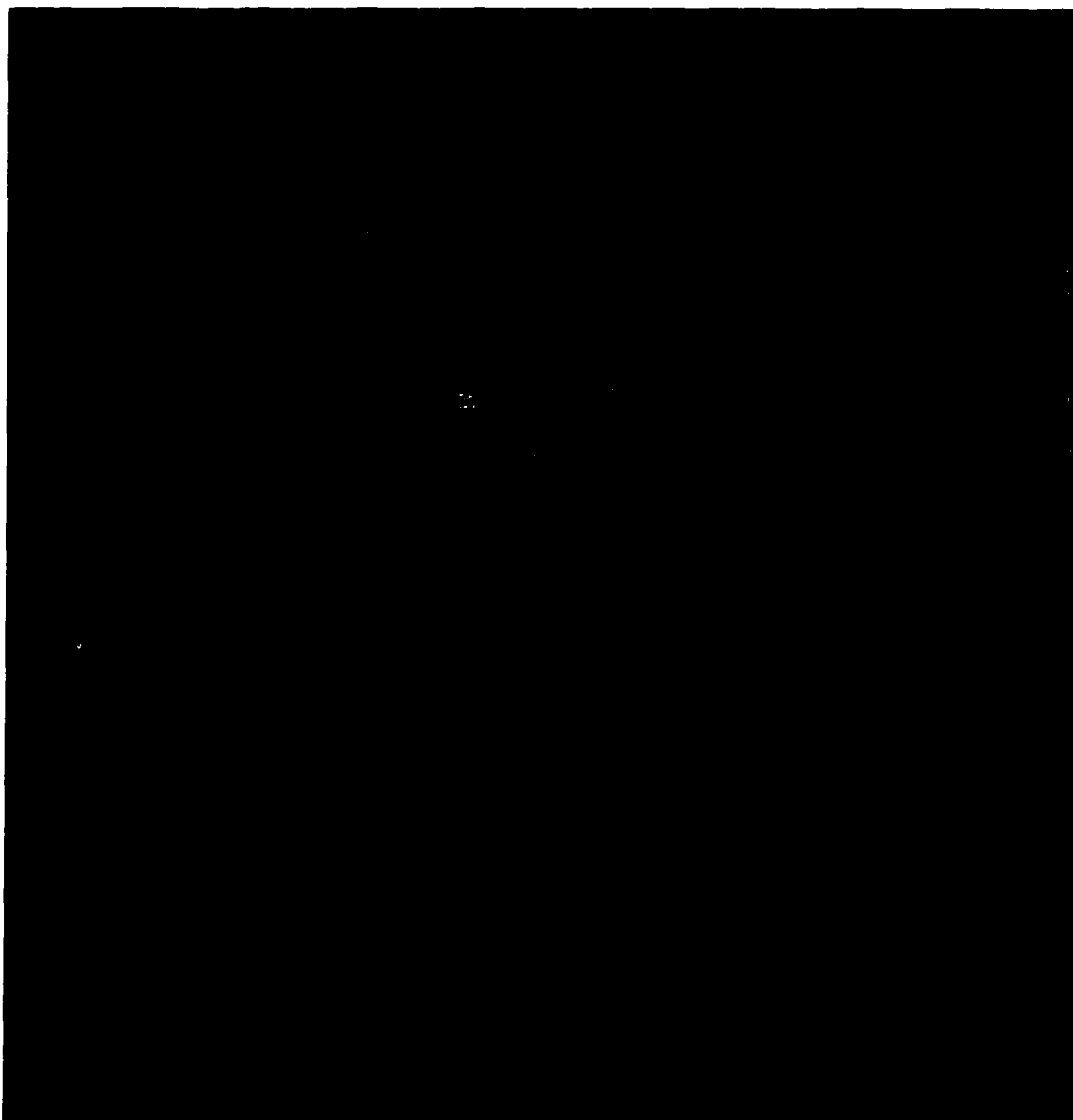


Figure 4.15: Another isosurface of the electrone charge at Γ . The red band contains the first two electrone bands, while the yellow band contains the second pair. Each surface contains four electrons and has a density of $3.5 \times 10^{-4} e/a.u.^3$.

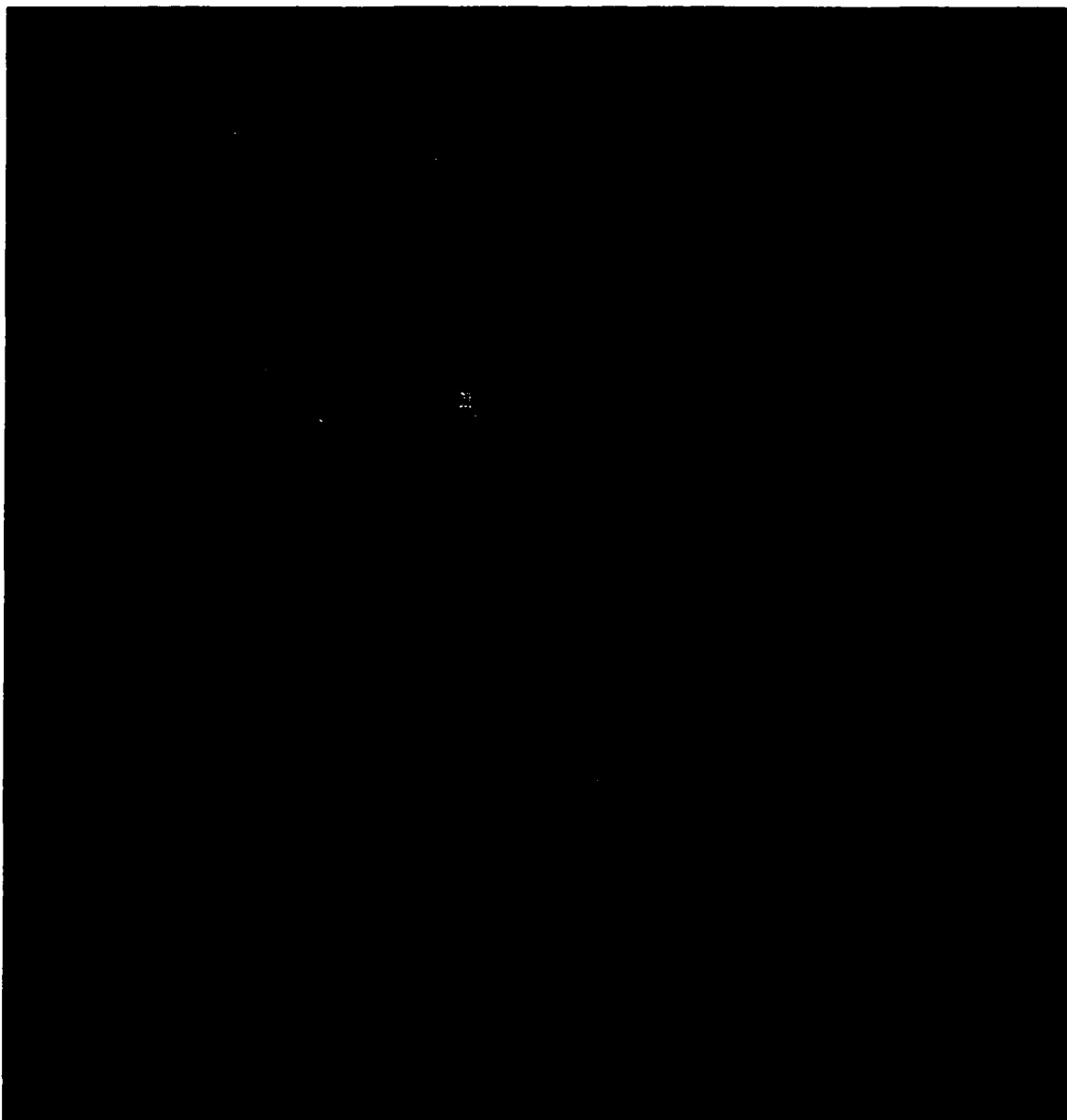


Figure 4.16: Another isosurface of the electrider charge at Γ . The red band contains the first two electrider bands, while the yellow band contains the second pair. Each surface contains four electrons and has a density of $4.5 \times 10^{-4} e/a.u.^3$.

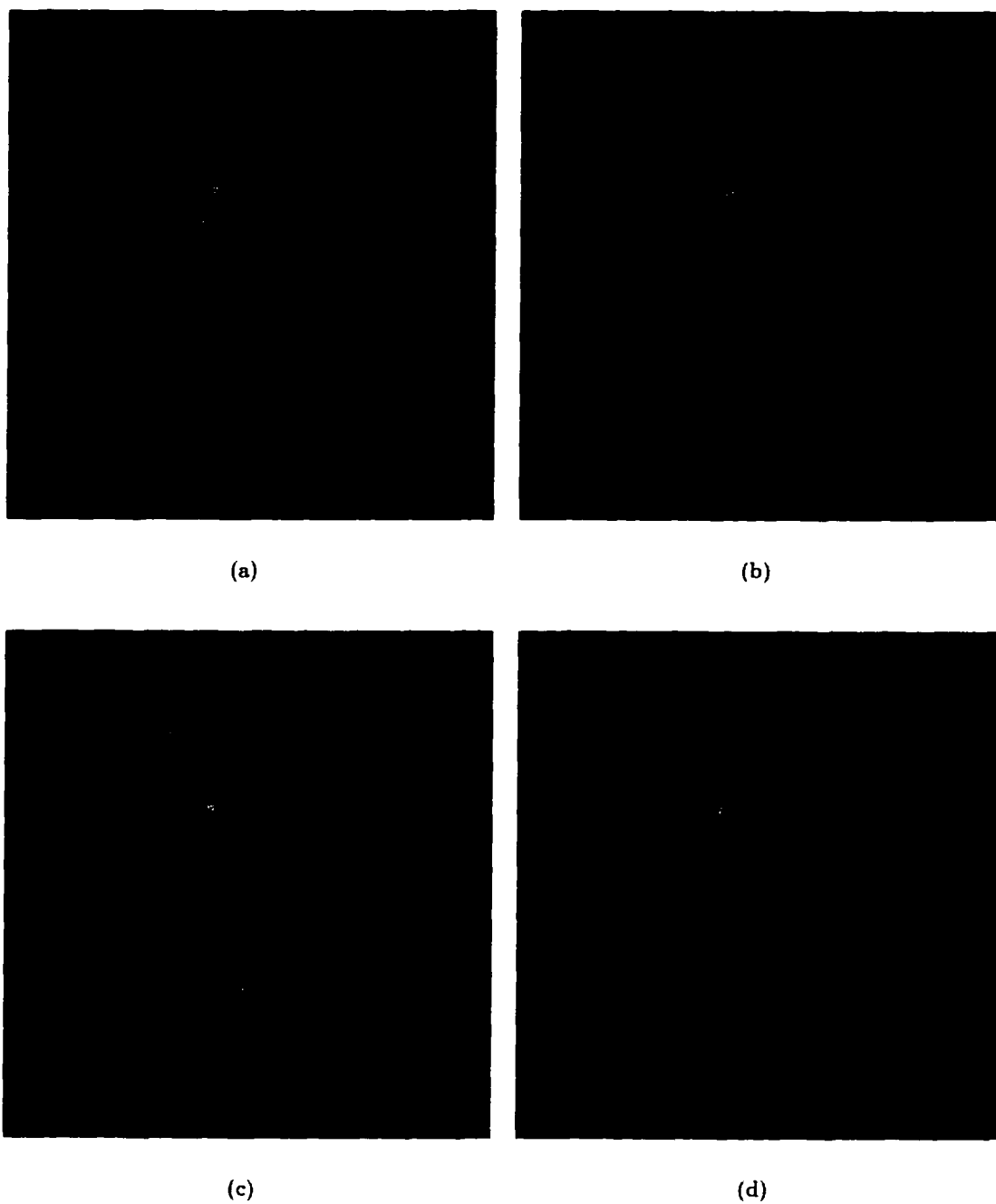


Figure 4.17: A sequence of isosurface plots of the potential in the cryptand calculation. Frames *a* and *b* have densities of 0.25 and 0.35 Ryd, while *c* and *d* are 0.40 and 0.48 Ryd.

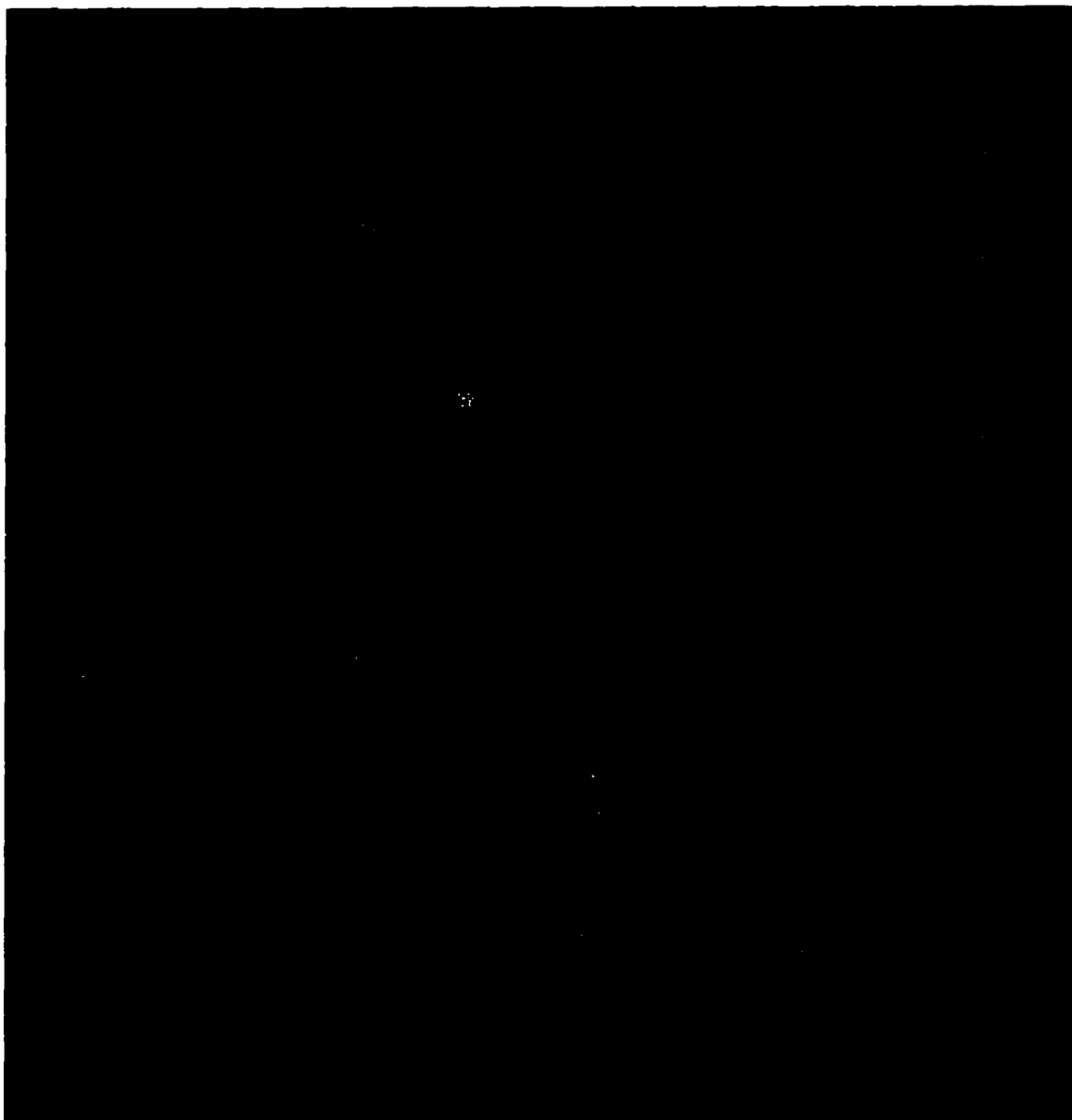


Figure 4.18: Here, the potential is compared to the charge of the first two bands at Γ . Note that the charge localizes in regions where the potential is strong. The density of the potential surface is 0.45 Ryd and the charge surface is at $3.0 \times 10^{-4} e/a.u.^3$.

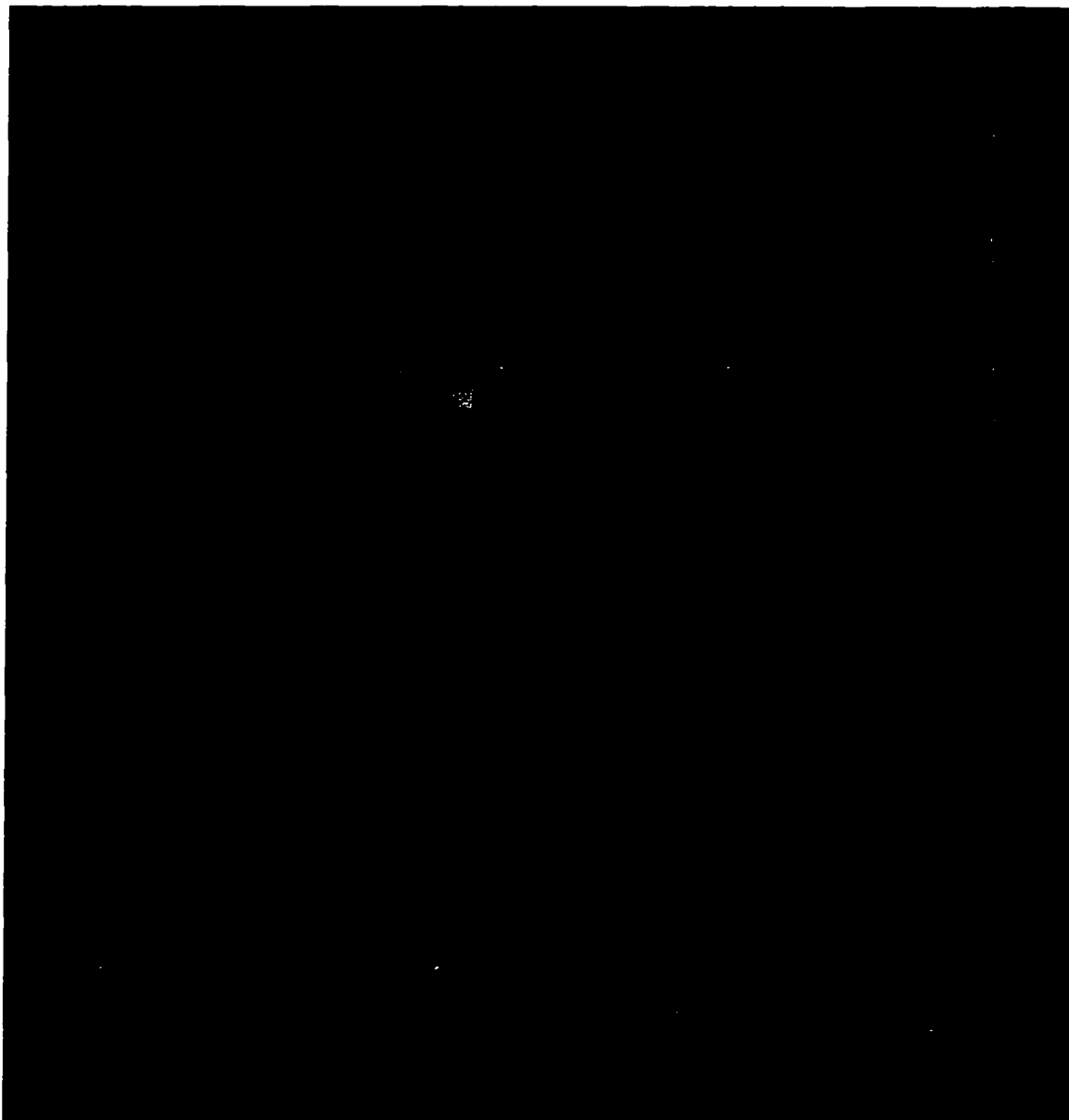


Figure 4.19: The potential at a density of 0.45 Ryd is compared to the second pair of bands at Γ , plotted at 3.0×10^{-4} e/a.u.³. Here, the charge tends to avoid the regions where the potential is strong.

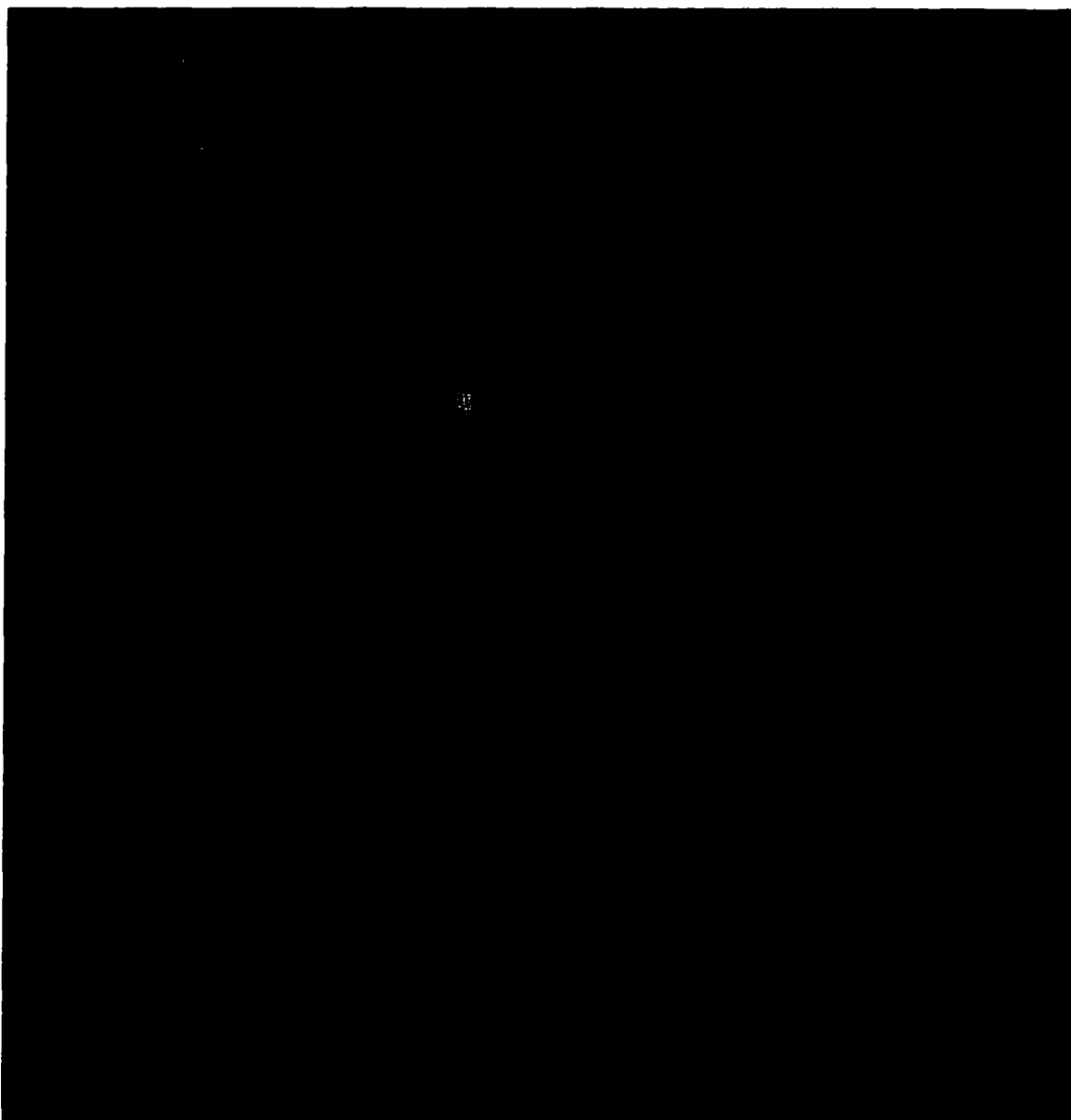


Figure 4.20: The potential at a density of 0.45 Ryd is compared second pair of electrider bands at Γ , plotted at 4.5×10^{-4} e/a.u.³. Here, the charge is primarily localized in regions of weak potential.

Figures 4.19 and 4.20, the potential is plotted against the second pair of bands at Γ . Here, it is seen that a large portion of the charge is located where the potential is relatively weak, and the channels connecting these bands do not follow the strong potential channels. This probably accounts in part for the higher energy of these unoccupied states.

In the preceding, we have seen that the occupied electrider states are localized in anionic-like states located in the cavities between the cryptand molecules, where the potential is most repulsive. As in the crown ether material, these anionic states can lower their kinetic energy by spreading out over the cavities. The degree of localization in the cavities varies somewhat as a function of k in the Brillouin zone.

These calculations unambiguously show the first direct computational evidence of the existence of localized, anionic-like states in the cavities between the cryptand molecules. This confirms many of the observations and expectations of the experimentalists. First, it is shown that, as in the cesium crown ethers, the electrider states exist in a region of strong potential energy, not in a potential well. Secondly, Figure 4.6, for example, demonstrates that pairs of localization regions are close enough to interact, but far enough apart that the interaction should be weak. Indeed, the channels connecting the regions primarily exist at lower charge densities. This system is predicted in our LDA calculations to be conducting, but this has yet to be fully verified experimentally.

Chapter 5

Conclusion

The projector basis method as presented here is a mixed basis hybrid of the APW and plane wave methods that capitalizes on the strengths of each. It keeps the scaling of the plane wave methods while retaining the ability to efficiently calculate first row elements and transition metals. The method is therefore able to perform calculations that are currently beyond the reach of both plane wave methods and the LAPW method.

The first two chapters served as an introduction to the rationale behind the method and the details of the implementation. In Chapter 3 the ability of the method to accurately reproduce the details of various test systems was demonstrated. This chapter also showed how the method behaves with different type of basis sets, and the effect these basis details have on the results. The final calculation in this chapter is the first large-scale test of the projector basis method. This showed that the method can not only handle large, complicated systems, but also that it is about 30% faster than the LAPW method on 15 atom systems.

In Chapter 4 the mixed basis method was used to carry out new and important studies on electrifieds, materials that are too complex to treat with conventional electronic

structure methods. In the cesium crown ether system it was shown that the anions are indeed electrons that are localized in a region where the potential is a maximum. Finally, a calculation of the lithium crown ether system is discussed. Here, again, the anionic electron is shown to be bound in a region of high potential, consistent with the cesium crown ether calculation. The experimentally determined properties, such as the weak interaction between the bound electrons, are verified. In addition, the LDA calculations predict that this system is a conductor, a fact that has not been determined experimentally.

In conclusion, the projector basis method has been shown to be a robust calculational tool that fits in the computational gap between the LAPW method and the modern plane wave methods.

Bibliography

- [1] R. Car and M. Parrinello, *Phys. Rev. Lett.* **55**, 2471 (1985).
- [2] M. C. Payne *et al.*, *Rev. Mod. Phys.* **64**, 1045 (1992).
- [3] S. Wei, Ph.D. thesis, The College of William & Mary, 1985.
- [4] P. Hohenberg and W. Kohn, *Phys. Rev. B* **136**, 864 (1964).
- [5] W. Kohn and L. J. Sham, *Phys. Rev. B* **140**, 1133 (1965).
- [6] V. Fock, *Z. Phys* **61**, 126 (1930).
- [7] D. Vanderbilt, *Phys. Rev. B* **41**, 7892 (1990).
- [8] K. Laasonen, R. Car, C. Lee, and D. Vanderbilt, *Phys. Rev. B* **43**, 6796 (1991).
- [9] K. Laasonen *et al.*, *Phys. Rev. B* **47**, 10142 (1993).
- [10] J. C. Slater, *Phys. Rev.* **51**, 846 (1937).
- [11] T. L. Loucks, *The Augmented-Plane-Wave Method* (Benjamin, New York, 1967).
- [12] O. K. Andersen, *Phys. Rev. B* **12**, 3060 (1975).
- [13] D. D. Koelling and G. O. Arbman, *J. Phys. F* **5**, 2041 (1975).

- [14] H. Krakauer, M. Posternak, and J. J. Freeman, *Phys. Rev. Lett.* **43**, 1885 (1979).
- [15] D. J. Singh, H. Krakauer, C. Haas, and A. Y. Liu, *Phys. Rev. B* **46**, 13065 (1992).
- [16] E. Antoncik, *J. Phys., Chem. Solids* **10**, 314 (1959).
- [17] J. C. Phillips and L. Kleinman, *Phys. Rev.* **116**, 287,880 (1959).
- [18] D. R. Hamann, M. Schlüter, and C. Chiang, *Phys. Rev. Lett.* **43**, 1494 (1979).
- [19] G. P. Kerker, *J. Phys. C* **13**, 189 (1980).
- [20] J. P. Perdew *et al.*, *Phys. Rev. B* **46**, 6671 (1992).
- [21] S. Baroni and P. Giannozzi, *Europhysics Lett.* **17**, 547 (1992).
- [22] L. Hedin and B. I. Lundqvist, *J. Phys. C* **4**, 2064 (1971).
- [23] D. M. Wood and A. Zunger, *J. Phys. A* **18**, 1343 (1985).
- [24] See, for example, W. H. Press, B. P. Flannery, S. A. Teukolsky, and W. T. Vetterling, *Numerical recipes in C* (Cambridge University Press, New York, 1988).
- [25] D. Singh, *Phys. Rev. B* **40**, 5428 (1989).
- [26] See, for example, J. S. Blakemore, *J. Appl. Phys.* **53**, R123 (1982).
- [27] C. S. Wang and B. M. Klein, *Phys. Rev. B* **24**, 3393 (1981).
- [28] S. Froyen and M. L. Cohen, *Phys. Rev. B* **28**, 3258 (1983).
- [29] T.-C. Chiang, J. A. Knapp, M. Aono, and D. E. Eastman, *Phys. Rev. B* **21**, 3513 (1980).
- [30] L. Ley *et al.*, *Phys. Rev. B* **19**, 600 (1974).

- [31] J. Ihm and J. D. Joannopoulos, *Phys. Rev. B* **24**, 4191 (1981).
- [32] D. J. Chadi and M. L. Cohen, *Phys. Rev. B* **8**, 5747 (1973).
- [33] H. J. Monkhorst and J. D. Pack, *Phys. Rev. B* **13**, 5188 (1976).
- [34] H. J. Monkhorst and J. D. Pack, *Phys. Rev. B* **16**, 1748 (1977).
- [35] E. Wimmer, H. Krakauer, M. Weinert, and A. J. Freeman, *Phys. Rev. B* **24**, 864 (1981).
- [36] S.-H. Wei and H. Krakauer, *Phys. Rev. Lett.* **Phys. Rev. Lett.**, 1200 (1985).
- [37] S.-H. Wei, H. Krakauer, and M. Weinert, *Phys. Rev. B* **32**, 7792 (1985).
- [38] S. C. Erwin, M. R. Pederson, and W. E. Pickett, *Phys. Rev. B* **41**, 10437 (1990).
- [39] W. E. Pickett and S. G. Louie, *Phys. Rev. B* **29**, 3470 (1984).
- [40] Z.-X. Shen and D. D. Dessa, *Electronic structure and photoemission studies of late transition-metal oxides—Mott insulators and high-temperature superconductors*, *Physica Reports* (1995).
- [41] J. Koringa, *Physica* **13**, (1946).
- [42] W. Kohn and N. Rostoker, *Phys. Rev.* **94**, 1111 (1954).
- [43] V. L. Moruzzi, J. F. Janak, and A. R. Williams, *Calculated Electronic Properties of Metals* (Pergamon, Elmsford, New York, 1974).
- [44] D. A. Papaconstantopoulos, *Handbook of the band structure of elemental solids* (Plenum, New York, 1986).

- [45] H. Maeda, Y. Tanaka, M. Fukutomi, and T. Asano, *Japan. J. Appl. Phys. Lett.* **27**, 209 (1988).
- [46] H. Heinrich, G. Kostorz, B. Heeb, and L. J. Gauckler, *Physica C* **224**, 133 (1994).
- [47] A. A. Levin, Y. I. Smolin, and Y. F. Shepelev, *J. Phys. C* **6**, 3539 (1994).
- [48] P. Aebi *et al.*, *Phys. Rev. Lett.* **72**, 2757 (1994).
- [49] J. M. Tarascon *et al.*, *Phys. Rev. B* **37**, 9382 (1988).
- [50] S. A. Sunshine *et al.*, *Phys. Rev. B* **38**, 893 (1988).
- [51] S. Massidda, J. Yu, and A. J. Freeman, *Physica C* **152**, 251 (1988).
- [52] M. S. Hybertsen and L. F. Mattheiss, *Phys. Rev. Lett.* **60**, 1661 (1988).
- [53] H. Krakauer and W. E. Pickett, *Phys. Rev. Lett.* **60**, 1665 (1988).
- [54] P. A. Sterne and C. S. Wang, *J. Phys. C* **21**, L949 (1988).
- [55] D. S. Dessau *et al.*, *Phys. Rev. Lett.* **71**, 2781 (1993).
- [56] D. J. Singh and W. E. Pickett, *Phys. Rev. B* **51**, 3128 (1995).
- [57] W. E. Pickett, *Rev. Mod. Phys.* **61**, 433 (1989).
- [58] R. H. Huang *et al.*, *Nature* **331**, 599 (1988).
- [59] A. Ellaboudy, J. L. Dye, and P. B. Smith, *J. Am. Chem. Soc.* **105**, 6490 (1983).
- [60] R. E. Peierls, *Quantum Theory of Solids* (Oxford University, London, 1956).
- [61] A. W. Overhauser, *Phys. Rev. B* **3**, 3173 (1971).
- [62] J. L. Dye and A. Ellaboudy, *Chem. Br.* **20**, 210 (1984).

- [63] J. L. Dye, *Scientific American* **66** (1987).
- [64] F. J. Tehan, B. L. Barnett, and J. L. Dye, *J. Am. Chem. Soc.* **96**, 7203 (1974).
- [65] G. Allan, M. G. D. Backer, M. Lannoo, and I. Lefebvre, *Europhys. Lett.* **11**, 49 (1990).
- [66] S. Matalon, S. Golden, and M. Ottolenghi, *J. Phys. Chem.* **73**, (1969).
- [67] M. T. Lok, F. J. Tehan, and J. L. Dye, *J. Phys. Chem.* **76**, 2975 (1974).
- [68] S. B. Dawes, D. L. Ward, R. H. Huang, and J. L. Dye, *J. Am. Chem. Soc.* **108**, 3534 (1986).
- [69] J. Dye, private communication to H. Krakauer (unpublished).
- [70] R. Huang and S. B. Dawes, private communication to H. Krakauer (unpublished).
- [71] B. M. Rode and S. V. Hannongbua, *Inorg. Chem. Acta* **96**, 91 (1985).
- [72] A. Pullman, C. Giessner-Prettre, and Y. V. Kruglyak, *Chem. Phys. Lett.* **35**, 156 (1975).
- [73] T. Yamabe, K. Hori, K. Akagi, and K. Fukui, *Tetrahedron* **35**, 1065 (1979).
- [74] K. Hori, H. Yamada, and T. Yamabe, *Tetrahedron* **39**, 67 (1983).
- [75] G. Wipff, P. Weiner, and P. Kollman, *J. Am. Chem. Soc.* **104**, 3231 (1982).
- [76] R. Perrin, C. Decoret, G. Bertholon, and R. Lamartine, *J. Chem. (Paris)* **7**, 263 (1983).
- [77] D. J. Singh, H. Krakauer, C. Haas, and W. E. Pickett, *Nature* **365**, 39 (1993).
- [78] N. W. Ashcroft and N. D. Mermin, *Solid State Physics* (Saunders College, Philadelphia, 1976).

- [79] J. S. Landers, J. L. Dye, A. Stacy, and M. J. Sienko, *J. Phys. Chem* **85**, 1096 (1981).
- [80] K. J. Moeggenborg, J. Papaioannou, and J. L. Dye, *Chem. Mater.* **3**, 514 (1991).
- [81] D. L. Ward, R. H. Huang, M. E. Kuchenmeister, and J. L. Dye, *Acta Crystallogr. C* **46**, 1831 (1990).
- [82] R. Rencsok, T. A. Kaplan, and J. F. Harrison, *J. Chem. Phys.* **93**, 5875 (1990).
- [83] R. E. Cohen, W. E. Pickett, and H. Krakauer, *Phys. Rev. Lett.* **62**, 831 (1989).
- [84] S. B. Dawes *et al.*, *J. Am. Chem. Soc.* **113**, 1605 (1991).

Vita

Christopher Haas was born in Fredericksburg, Virginia on June 19, 1967. He earned a B.S. in physics from Roanoke College in May of 1989, and received a Masters in Arts from the College of William and Mary in June of 1991. He completed the requirements for Ph.D. in physics at the College of William and Mary in August of 1996.